Monthly Notices
of the
ROYAL ASTRONOMICAL SOCIETY

MNRAS **490,** 5317–5334 (2019)
Advance Access publication 2019 October 14

doi:10.1093/mnras/stz2850

A SCUBA-2 selected *Herschel*-SPIRE dropout and the nature of this population

J. Greenslade,[1] E. Aguilar,[2] D. L. Clements,[1]★ H. Dannerbauer,[3,4] T. Cheng,[1] G. Petitpas,[5] C. Yang,[6] H. Messias,[6,7] I. Oteo,[8,9] D. Farrah,[10,11] M. J. Michałowski,[12] I. Pérez Fournon,[3,4] I. Aretxaga,[2] M. S. Yun,[13] S. Eales,[14] L. Dunne,[8,14] A. Cooray,[15] P. Andreani,[9] D. H. Hughes,[2] M. Velázquez,[2] D. Sánchez-Argüelles[2] and N. Ponthieu[16]

[1]*Astrophysics Group, Blackett Laboratory, Imperial College London, London SW7 2AZ, UK*
[2]*Óptica y Electrónica (INAOE), Instituto Nacional de Astrofísica, Luis Enrique Erro 1, Sta. Ma. Tonantzintla, Puebla 72840, México, USA*
[3]*Instituto de Astrofísica de Canarias (IAC), Tenerife, E-38205 La Laguna, Spain*
[4]*Dpto. Astrofísica, Universidad de La Laguna, Tenerife, E-38206 La Laguna, Spain*
[5]*Harvard-Smithsonian Center for Astrophysics, 60 Garden Street, Cambridge, MA 02138*
[6]*European Southern Observatory, Alonso de Córdova 3107, Vitacura, Casilla 19001 Santiago, Chile*
[7]*Joint ALMA Observatory, Alonso de Córdova 3107, Vitacura, Santiago 763-0355, Chile*
[8]*Royal Observatory, Institute for Astronomy, University of Edinburgh, Blackford Hill, Edinburgh EH9 3HJ, UK*
[9]*European Southern Observatory, Karl-Schwarzschild-Strasse 2, Garching D-85748, Germany*
[10]*Department of Physics and Astronomy, University of Hawaii, 2505 Correa Road, Honolulu, HI 96822, USA*
[11]*Institute for Astronomy, University of Hawaii, 2680 Woodlawn Drive, Honolulu, HI 96822, USA*
[12]*Faculty of Physics, Astronomical Observatory Institute, Adam Mickiewicz University, ul. Słoneczna 36, Poznań, PL-60-286, Poland*
[13]*Department of Astronomy, University of Massachusetts, Amherst, MA 01003, USA*
[14]*School of Physics and Astronomy, Cardiff University, The Parade, Cardiff CF24 3AA, UK*
[15]*Department of Physics and Astronomy, University of California, Irvine, CA 92697, USA*
[16]*Institut de Planétologie et d'Astrophysique de Grenoble, 414 Rue de la Piscine, Saint-Martin-d'Hères, F-38400, France*

Accepted 2019 October 4. Received 2019 September 4; in original form 2019 January 9

ABSTRACT

Dusty star-forming galaxies (DSFGs) detected at $z > 4$ provide important examples of the first generations of massive galaxies. However, few examples with spectroscopic confirmation are currently known, with Hershel struggling to detect significant numbers of $z > 6$ DSFGs. NGP6_D1 is a bright 850 μm source (12.3 $\pm$ 2.5 mJy) with no counterparts at shorter wavelengths (a SPIRE dropout). Interferometric observations confirm it is a single source, with no evidence for any optical or NIR emission, or nearby likely foreground lensing sources. No $>3\sigma$ detected lines are seen in both LMT Redshift Search Receiver and IRAM 30 m EMIR spectra of NGP6_D1 across 32 GHz of bandwidth despite reaching detection limits of $\sim 1\,\mathrm{mJy}/500\,\mathrm{km\,s^{-1}}$, so the redshift remains unknown. Template fitting suggests that NGP6_D1 is most likely between $z = 5.8$ and 8.3. SED analysis finds that NGP6_D1 is a ULIRG, with a dust mass $\sim 10^8$–10^9 $\mathrm{M_\odot}$ and a star-formation rate of $\sim$500 $\mathrm{M_\odot\ yr^{-1}}$. We place upper limits on the gas mass of NGP6_D1 of $M_{H2} < (1.1 \pm 3.5) \times 10^{11}$ $\mathrm{M_\odot}$, consistent with a gas-to-dust ratio of $\sim$100–1000. We discuss the nature of NGP6_D1 in the context of the broader sub-mm population, and find that comparable SPIRE dropouts account for $\sim$20 per cent of all SCUBA-2 detected sources, but with a similar flux density distribution to the general population.

Key words: galaxies: high-redshift – galaxies: photometry – galaxies: starburst – submillimetre: galaxies.

1 INTRODUCTION

The high-redshift ($z \geq 4$) population of dusty star-forming galaxies (DSFGs) remains poorly constrained. Models have consistently

★ E-mail: d.clements@imperial.ac.uk

© 2019 The Author(s)
Published by Oxford University Press on behalf of the Royal Astronomical Society

Downloaded from https://academic.oup.com/mnras/article/490/4/5317/5587004 by guest on 23 June 2022

been unable to reproduce the observed number counts of the red, $z \geq 4$ DSFGs (Dowell et al. 2014; Asboth et al. 2016; Ivison et al. 2016), and questions remain about whether DSFGs significantly contribute to the global star-formation rate (SFR) density at $z > 3$ (Rowan-Robinson et al. 2016; Liu et al. 2017; Novak et al. 2017) or not (Koprowski et al. 2017; Michałowski et al. 2017). It has been claimed that we can neither rule out a *negligible* or *dominant* contribution to this SFR-density from DSFGs at $z > 3.5$ (Casey et al. 2018). Whether these mismatches are due to observational issues such as blending (e.g. Scudder et al. 2016) or lensing, or are due to the assumptions that have gone into the numerical models (e.g. Béthermin et al. 2017) remains unclear. Since we expect these sources to evolve into present-day elliptical galaxies in massive clusters (Wilkinson et al. 2016), the highest redshift DSFGs likely also trace the most massive dark matter haloes in the early Universe. The statistical characterization of this population is therefore a key goal for observational astronomy.

Partially, the lack of constraints on high-z DSFGs comes down to the difficulty of detecting them. Only a handful of DSFGs at $z \geq 4$ have spectroscopic confirmation (Capak et al. 2008; Daddi et al. 2008; Coppin et al. 2009; Riechers et al. 2010; Capak et al. 2011; Cox et al. 2011; Combes et al. 2012; Walter et al. 2012; Riechers et al. 2013; Dowell et al. 2014; Yun et al. 2015; Asboth et al. 2016; Ivison et al. 2016; Oteo et al. 2016a,b; Fudamoto et al. 2017; Marrone et al. 2017; Riechers et al. 2017; Strandet et al. 2017). The selection criteria used for these high-z DSFGs is varied: some are selected through FIR colours (Riechers et al. 2013; Dowell et al. 2014; Asboth et al. 2016; Ivison et al. 2016; Zavala et al. 2018), whilst others use mm selection (Strandet et al. 2017), and still others sub-mm wavelengths (Walter et al. 2012). Even after candidate selection, spectroscopic confirmation remains difficult, often requiring counter-part identification in optical, near or mid-infrared or radio bands, which do not benefit from the extremely negative *k*-correction that applies to the sub-mm and mm bands.

Most literature redshift distributions of far-infrared (FIR) and sub-mm selected DSFGs find a median redshift of $z \sim 2$, with typical interquartile ranges of $z = 1.8$–2.8 (Chapman et al. 2005; Wardlow et al. 2011; Simpson et al. 2017; Smith et al. 2017; Bakx et al. 2018). Consistently, around 30 per cent of DSFGs have no optical, NIR, MIR, or radio counterparts in these literature studies, and are routinely assumed to be high redshift. Surveys in the mm, such as the South Pole Telescope (SPT; Carlstrom et al. 2011) or AZTEC surveys (Chapin et al. 2009; Vieira et al. 2013; see also Miettinen et al. 2015), support this – finding a median redshift distribution between 2.6 and 3.1, suggestive of a population of high-z sources whose specific redshifts are difficult to confirm or constrain.

Arguably the most successful selection technique for high-z DSFGs has been the selection of *Herschel*-SPIRE 500 μm riser sources ($S_{500} > S_{350} > S_{250}$), hereafter referred to as 500 μm risers. This selection has led to spectroscopic confirmation of numerous $z > 4$ DSFGs (Dowell et al. 2014; Asboth et al. 2016; Ivison et al. 2016), and two $z > 6$ sources (Riechers et al. 2013; Zavala et al. 2018). Whilst impressive, it should be noted that these results are taken from over 1000 deg^2 of *Herschel*-SPIRE data, and effectively set lower limits for the number counts of *Herschel*-SPIRE detectable $z > 6$ DSFGs of $\gtrsim 2 \times 10^{-3}$ deg^{-2}. Furthermore, given the confusion limited 3σ SPIRE detection threshold of around 20–30 mJy, a source must still be, in general, highly luminous ($\sim 10^{13}$ L$_\odot$) to be detected by SPIRE at $z > 4$, a problem which gets worse at higher redshifts. Indeed, both of the two SPIRE detected $z > 6$ DSFGs (Riechers et al. 2013; Zavala et al. 2018) are observed to have FIR luminosities $>10^{13}$ L$_\odot$ [though both are additionally lensed, and only HFLS3 (Riechers et al. 2013) has a FIR luminosity intrinsically $>10^{13}$ L$_\odot$].

Until recently, limited field sizes and depths at sub-mm and mm wavelengths have meant that systematic searches for the rarer $z > 4$ DSFGs or sub-millimetre galaxies (SMGs) have been restricted to 500 μm risers, lensed sources, or serendipitous discovery. Now, however, with larger ~ 1 deg^2 surveys at 850 μm such as the S2-CLS and S2-COSMOS surveys (Geach et al. 2017; Simpson et al. 2019), which overlap with the larger *Herschel*-SPIRE extragalactic fields, new colour selections can be made. Perhaps the most obvious high-z selection is to extend the 500 μm risers to 850 μm risers ($S_{850} > S_{500}$). At a minimum, this would require detection at both 850 μm and at least in the 500 μm band of SPIRE to ensure the riser condition is fulfilled. To date, only one spectroscopically confirmed 850 μm riser is known, ADFS-27 at $z = 5.655$ (Riechers et al. 2017), suggesting this selection is reasonably successful at selecting the highest redshift DSFGs. However, ADFS-27 is only just detected at 500 μm in SPIRE,[1] with a flux density of $S_{500} = 24.0 \pm 7.5$, and is not detected in either of the other two SPIRE bands.

The apparent rarity of 850 μm risers detected at both 500 and 850 μm makes systematic selection of high-z DSFGs difficult. However, catalogues of sources from these new, > 1 deg^2 fields at 850 μm have revealed a population of reasonably bright (> 5 mJy) 850 μm sources that are not only *not* detected at other optical, near or mid-infrared, or radio wavelengths, but are additionally undetected in any of the three *Herschel*-SPIRE bands. These 'SPIRE dropouts' are difficult to explain, as, unless the peak of the thermal emission lies near 500–850 μm, we would expect to detect them in the shorter wavelength SPIRE bands. The nature of these dropouts is uncertain, but the two simplest explanations are that this population is either very high redshift, with a median redshift higher than the 500 μm risers, or that they represent a cooler population hitherto undiscovered at $z > 4$. Both of these solutions are interesting in their own right, indicating that these dropouts are worthy of further study.

In this paper, we detail NGP6_D1, a serendipitous SPIRE dropout first identified in 2014, our subsequent follow up, and our interpretation of what this source, and others like it, represent. Given the numerous observations taken of NGP6_D1, we start in Section 2 by providing an overview of all the observations that have taken place. We then present the photometric and spectroscopic analysis for this source in Section 3. In Section 4, we discuss NGP_D1 in the broader context of the current searches for high-z DSFGs, including comparisons to the literature, and examine how numerous NGP6_D1-like objects might be, and what they might represent. Finally, we summarize and conclude our results in Section 5. Throughout this paper, we assume the concordance Λ-CDM cosmology, with $H_0 = 67.74$ km s^{-1} Mpc^{-1}, $\Omega_\Lambda = 0.69$, and $\Omega_m = 0.31$.

2 DATA

NGP6_D1 was initially detected serendipitously, as part of a follow-up program of *Planck* selected *Herschel* overdensities (Clements et al. 2014; Greenslade et al. 2018; Cheng et al. 2019). A region in the north galactic pole (NGP), initially observed by *Herschel* as part of the H-ATLAS project (Eales et al. 2010; Bourne et al.

[1] When including a constant confusion noise of 7 mJy, typical of the SPIRE maps (Dowell et al. 2014; Asboth et al. 2016).

Downloaded from https://academic.oup.com/mnras/article/490/4/5317/5587004 by guest on 23 June 2022

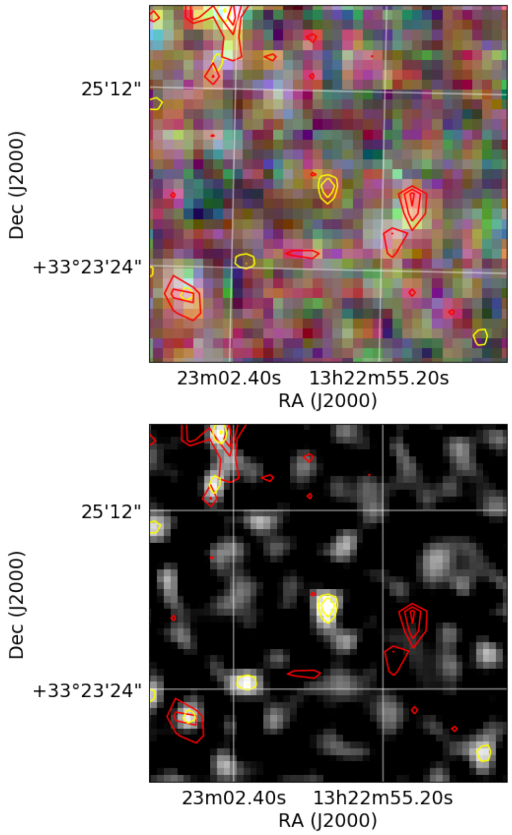


Figure 1. *(Top)* A 2.5 × 2.5 arcmin^2 RGB (500, 350, and 250 μm) *Herschel*-SPIRE image of the region around NGP6_D1. Red contours show the 3, 4, and 5σ detection levels for the 500 μm band, whilst yellow contours show the 3, 4, and 5σ detection levels for the SCUBA-2 850 μm band. *(Bottom)* The SCUBA-2 image of the same region, with contours indicating the same as the top image.

2016; Valiante et al. 2016; Smith et al. 2017), was observed by the SCUBA-2 instrument on the JCMT at 850 μm (Project ID: M13AU12) between 2013 April 8th and 12th. The observations used a CV_DAISY pattern, and reached an approximately uniform rms of ∼3 mJy over a 2 arcmin radius. The atmospheric opacity on the nights varied between $\tau_{225\,\mathrm{GHz}} = 0.05$ and 0.12, and pointing was done using the quasar 1308+326. The data were reduced using the SCUBA-2 pipeline SMURF (Chapin et al. 2013), and for calibration the standard 850 μm flux conversion factor (FCF) of 537 Jy pW^{-1} was used.

This map revealed a 12.3 ± 2.5 mJy SCUBA-2 source detected at 4.9σ at position RA : 13:22:57.91, Dec. : +33:24:14.05. After examining the *Herschel*-SPIRE maps at the position of this SCUBA-2 source, we found no evidence of any emission in any of the three SPIRE bands, with measured flux densities of −2.31 ± 5.54, 2.30 ± 5.84 and 7.49 ± 7.35 mJy at 250, 350, and 500 μm, respectively. Given a 3σ detection limit, this places upper limits on the *Herschel*-SPIRE flux density of NGP6_D1 of 16.5, 17.4, and 22.0 mJy at 250, 350, and 500 μm. Bootstrapping the SCUBA-2 data revealed that the source was likely real, and still detected to at least a 3σ level when randomly discarding half the data. The nearest detected *Herschel* source lies 45 arcsec away from the peak of the SCUBA-2 emission. A *Herschel* RGB (500, 350, 250 μm) map with the contours overlaying the SCUBA-2 position is shown in Fig. 1. As this source has effectively dropped out of the SPIRE bands, we herein refer to it as a SPIRE dropout, with the designation NGP6_D1.

Table 1. The FIR, sub-mm, mm, and radio photometry of NGP6_D1. Flux densities are given in mJy. These measurements come from *Herschel*-SPIRE (250, 350, 500 μm), SMA (870 μm, 1.1 mm), NIKA (1.25 and 2.0 mm), NOEMA (2.8 mm), and VLA (6 GHz) at the position of the source as derived from the SMA maps. Square brackets indicate 3σ upper limits in the case of non-detection in the SPIRE maps; specific SPIRE values at the position of the source are included as these are used for template fitting to constrain the peak of the thermal emission.

Band	Flux [mJy]
250 μm	−3.3 ± 4.2 [<12.6]
350 μm	3.0 ± 4.4 [<13.2]
500 μm	7.7 ± 8.9 [<26.7]
850 μm	12.3 ± 2.5
870 μm	8.0 ± 1.3
1.1 mm	5.9 ± 1.1
1.25 mm	3.97 ± 0.43
2 mm	1.04 ± 0.12
2.8 mm	0.60 ± 0.04
6 GHz	(1.69 ± 0.4) × 10^{-2}

In this Section, we detail our photometric and spectroscopic follow-up observations of this isource, with a summary of our observations available in Table 1.

2.1 Photometric observations

2.1.1 SMA

We undertook observations using the Sub-Millimeter Array (SMA) in extended configuration at 870 μm and 1.1 mm on 2019 March 29th and 23rd, respectively (Project ID: 2014A-S092). The bandpass calibrator was 3c84, while Callisto was used as flux density calibrator, and the quasars 1310+323 and 1224+213 were used as gain calibrators. The data was reduced with a combination of both IDL and MIRIAD using natural weighting to optimize the point-source sensitivity. The smaller 870 μm synthesized beam had semimajor and semiminor axis of 0.″78 × 0.″47, and the maps reached 1σ rms of 1.31 and 1.36 mJy in the 870 μm and 1.1 mm bands, respectively.

In both the 870 μm and 1.1 mm maps, a source was found, well within the ∼13 arcsec full-width half-maximum (FWHM) SCUBA-2 beam, and with position RA: 13:22:57.842, and Dec.: +33:24:16.56. The measured flux densities were 8.03 ± 1.31 mJy and 5.96 ± 1.36 mJy at 870 μm and 1.1 mm, respectively. The 870 μm flux density values are consistent within 2σ with the observed SCUBA-2 flux density. The SMA image of NGP6_D1 at 870 μm is plotted in Fig. 2, alongside the contours at both 1.1 mm from the SMA and 850 μm from SCUBA-2. The *Herschel* measured flux densities at the position of the SMA source are −3.34 ± 4.16 mJy, 2.98 ± 4.42 mJy, and 7.70 ± 8.90 mJy in the 250, 350, and 500 μm bands, respectively.

2.1.2 NIKA

NGP6_D1 was observed on the IRAM 30 m telescope using the NIKA (Monfardini et al. 2010) instrument at 1.25 and 2 mm (beamsizes of 12 and 17.5 arcsec) between the 2015 February 8th and 9th (Project ID: 227-14) for 2 hr, reaching rms values of ∼0.4 and 0.1 mJy in the two bands, respectively. Tau values

Downloaded from https://academic.oup.com/mnras/article/490/4/5317/5587004 by guest on 23 June 2022

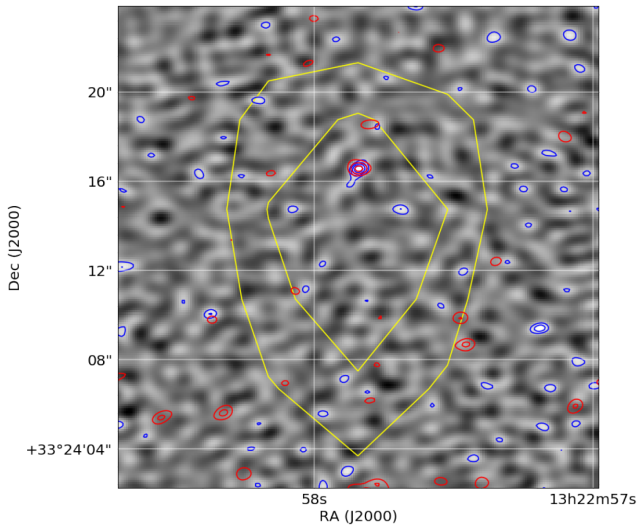


Figure 2. The SMA 345 GHz (870 μm) map of NGP6_D1, overlaid with SCUBA-2 S/N contours (yellow) in steps of 3, 4, and 5σ, and SMA 870 μm S/N contours (blue) and SMA 1.1 mm contours (blue), both in steps of 2, 3, 4, and 5σ.

ranged between $\tau_{225\,\mathrm{GHz}} = 0.01$ and 0.28 with an average of 0.15, but this was generally split between a high opacity $\tau_{225} > 0.1$ and low opacity $\tau_{225} < 0.1$ grouping. The data were reduced by the NIKA team's pipeline, using a 'point source oriented' reduction. A single source was found at the position of the SMA object, with a 1.25 mm flux density of 3.97 $\pm$ 0.43 mJy and a 2 mm flux density of 1.04 $\pm$ 0.12 mJy. The fluxes were found to be consistent when using only the high tau or low-tau data sets, but there remains a 10–15 per cent uncertainty on the flux calibration. The 1.25 mm flux from NIKA appears inconsistent with the 1.1 mm flux from the SMA, with the SMA 1.1 mm measurement 50 per cent higher than the NIKA 1.25 mm measurement.

2.1.3 VLA

The region around NGP6_D1 was observed by the Very Large Array (VLA) on 2016 December 17 (Project ID VLA/2016-00-110; PI David Clements) for 1.75 hr. This observation was in *C*-band (6 GHz, 50 mm), and in A-configuration, with a synthesized beamwidth of 0.33 $\times$ 0.33 arcsec^2. For bandpass and flux calibration, 3C 286 (1331+305) was used, while J1310 + 3220 was the phase calibrator. Data were reduced using the Common Astronomy Software Application (CASA) package (McMullin et al. 2007), version 4.7.0. Small amounts of radio frequency interference (expected to be around $\sim$15 per cent) were detected and flagged automatically during the reduction process. The field is cleaned using Briggs (robust) weighting, with a robust parameter of 0, to provide a good balance between angular resolution and sensitivity to all sources in the field. These radio observations were taken on a number of protocluster candidates, and the full results will be presented in a future paper (Cheng et al. in preparation).

We examined the map around the position of NGP6_D1 and detected a 4.5σ source, with a 6 GHz flux density of 16.9 $\pm$ 3.7 Jy, with a position only 0.05 arcsec from the SMA position of NGP6_D1. Assuming the radio emission is concurrent with the FIR emission, our VLA map localizes our source to a 0.33 $\times$ 0.33 arcsec^2 area on the sky.

2.1.4 Ancillary data from SDSS, UKIDSS, and WISE

The area around NGP6_D1 was observed in both the Sloan Digital Sky Survey (SDSS; Abolfathi et al. 2017) and UKIRT Infrared Deep Sky Survey (UKIDSS; Lawrence et al. 2006; Warren et al. 2006) in the optical and NIR. These observations reach approximate AB magnitude limits of u : 22.0, g : 22.2, r : 22.2, i : 21.3, and z: 20.5 in SDSS, and Vega limits of Y : 20.2, J : 19.6, H : 18.8, and Ks : 18.2 from UKIDSS. Though there are two SDSS galaxies approximately 8 and 11 arcsec to the north of the SMA positions of NGP6_D1, there is no current evidence of any optical counterpart, or indication that NGP6_D1 is being lensed by any foreground source. We do note, however, that deeper images in the optical or NIR may change this.

2.2 Spectroscopic observations

Through both photometric analysis and template fitting of the above data (see Section 3 for more details), we estimate that the most likely redshift for NGP6_D1 is between $z = 5.8$ and 8.3. To determine a redshift, we opted to target ^{12}CO lines (hereafter, referenced as simply CO). The CO(J = 1 $\rightarrow$ 0) transmission occurs at a rest-frame frequency of 115.27 GHz ($\sim$ 2600 μm), with subsequent CO[J = n $\rightarrow$ (n$-$1)] transmissions taking place at n $\times$ 115.27 GHz. At $z > 5$, we would therefore expect adjacent CO lines to be spaced out by <20 GHz. Blind redshift searches on SMGs targeting CO lines have been performed before, and to a reasonable level of success (Weiß et al. 2013; Dannerbauer et al. 2014; Fudamoto et al. 2017). In this Sub-section, we report our spectroscopic observations of NGP6_D1 using both the Redshift Search Receiver (RSR) and EMIR instruments, and our resulting spectra from both instruments are shown in Fig. 3.

2.2.1 Redshift Search Receiver

The RSR (Erickson et al. 2007; Goeller 2008) is the wide-band 3 mm spectrograph currently installed on the 50 m Large Millimeter Telescope (LMT; Hughes et al. 2010). It has a spectral resolution of 31 MHz or $\sim$100 km s^{-1} at 92 GHz, and an instantaneous frequency coverage of 73–111 GHz. The RSR follow up of NGP6_D1 was conducted on the early science phase with a 32 m dish configuration, which provides a spatial resolution of 25 arcsec at 92 GHz. The opacity $\tau_{225\,\mathrm{GHz}}$ ranged between 0.10 and 0.27 with an average $T_{sys} \sim 100$ *K* over the six observation nights (2016 January 29 and February 1–3, 7, and 8). The total on-source integration time on NGP6_D1 was 9 hr (108 spectra $\times$ 300 s each). Pointing corrections were made by observing 1224+213 or 1310 + 323 every hour.

The individual observations are transformed into the frequency domain, baselined, and co-added using DREAMPY (Data Reduction and Analysis Methods in PYTHON2), written by Gopal Narayanan, to generate the spectrum. The final spectrum was obtained by co-adding the best data, defined as all the individual spectra which do not have large structure systematics in the baseline due to low-frequency noise (electronic drift). After co-addition the data are smoothed with a three channel boxcar filter. Additionally, we smooth the co-added spectrum to match a velocity resolution of 500 km s^{-1}, typical of other high-z DSFGs (Bothwell et al. 2013; Riechers et al. 2013; Aravena et al. 2016; Strandet et al. 2017; Yang et al. 2017; Zavala et al. 2018). To convert from antenna temperature to flux units, we use a factor of 6.4 Jy K^{-1} for $\nu \leq 92$ GHz and 7.6 Jy K^{-1} for $\nu > 92$ GHz.

Downloaded from https://academic.oup.com/mnras/article/490/4/5317/5587004 by guest on 23 June 2022

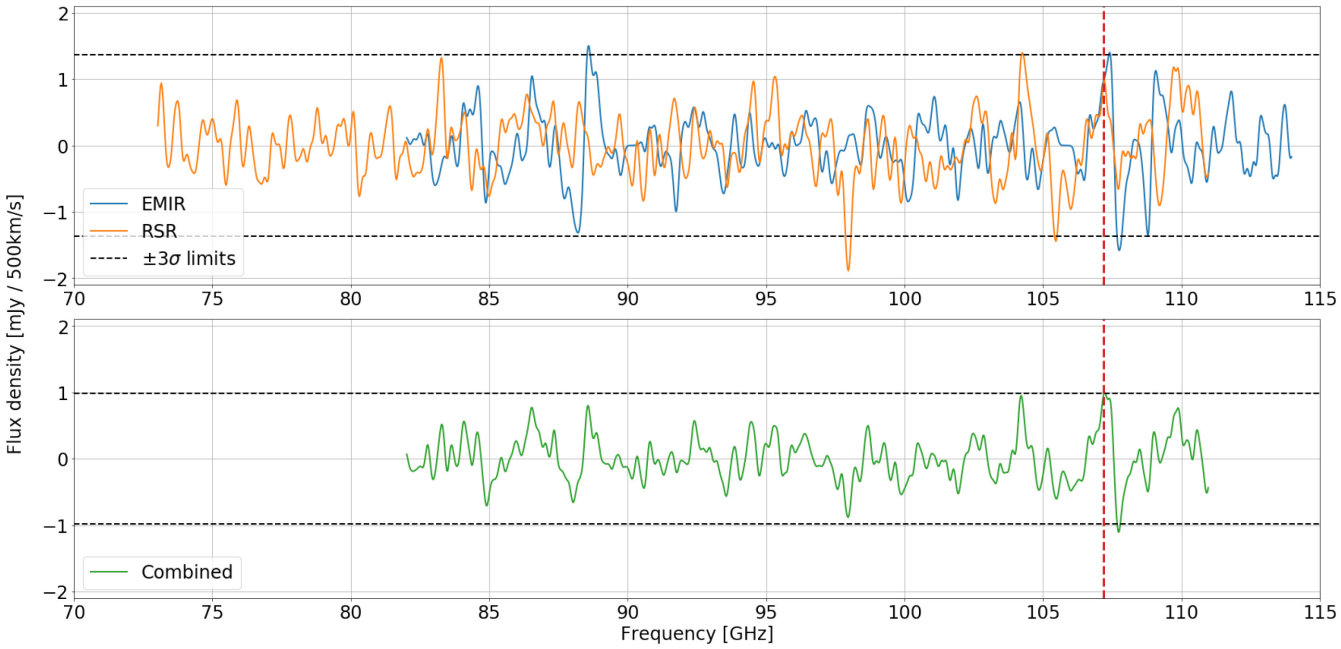


Figure 3. Spectra of NGP6_D1 from the RSR and EMIR (top), and the spectra from combining the data from the two instruments (bottom). The data is smoothed with a Gaussian with a velocity width of 500 km s^{-1} in all three cases. The dashed horizontal black lines show the $\pm 3\sigma$ limits for both the RSR, EMIR and combined, whilst the dashed red vertical line shows the position of a 3.03σ line at 107.2 GHz when the data from the RSR and EMIR are combined and smoothed to a velocity width of $\sim$500 km s^{-1}.

As can be seen in Fig. 3, there is a $>3\sigma$ feature detected at 104.28 GHz in the RSR spectrum, and a second line marginally detected to a 2.8σ level at 83.2 GHz. This could reasonably correspond to a $z \sim 4.53$ SMG, and template cross-correlation analysis (i.e. Yun et al. 2015) suggests a combined detection S/N of 5.5 in support of this redshift solution. However, as discussed below, neither candidate line is detected in EMIR, and there are additionally two frequencies that are negatively detected as strongly as these candidate lines. Further evidence would be needed before any definite conclusion as to the reality of these lines can be made, and we therefore conclude that there is no strong evidence for any detected features in the RSR spectrum.

2.2.2 *EMIR*

NGP6_D1 was observed for a total of 61 hr with the EMIR instrument on the IRAM 30 m telescope (Project ID: 199-15) to search for ^{12}CO lines. Two set-ups covered a total of 31 GHz (83–114 GHz) of frequency space to an rms of 0.06 mK ($\sim$0.42 mJy), with two small 1GHz gaps at 90 and 105.5 GHz due to different set-ups. The observations ran from the 2016 March 14th–20th, with tau values varying from 0.01 to 0.5, and an average of $\tau_{225} \sim 0.2$. Both WILMA and FTS200 were used as back-ends, with FTS200 covering a larger 32 GHz of bandwidth compared to WILMA. The data were reduced using CLASS and PYTHON, and smoothing our data to between 100 and 500 km s^{-1}, we achieved an rms of between 0.1 and 0.07 mK, corresponding to a line sensitivity of 0.7–0.5 mJy. No evidence of any lines is seen in the WILMA back-end, but FTS200 covering a larger bandwidth detects two $\sim 3\sigma$ peaks, one of which appears concurrent with a peak in the RSR spectra.

2.2.3 *NOEMA*

Both EMIR and the RSR see a marginal line at 107.2 GHz, with $\sim 3\sigma$ and 1.7σ detections, respectively. Combining these results together, as seen in Fig. 3, results in a 3.2σ detection of this line. We therefore obtained NOEMA DDT to follow up this candidate line.

The NOEMA Interferometer is a millimeter array located on the Plateau de Bure in the French Alps. A spectral line scan of NGP6_D1 was carried out in 2017 January (DDT E16AD: PI J. Greenslade) with 7 (2017 January 20) and 8 antennas (2017 January 21) in D configuration to search for the possible line at 107.2 GHz. The Wide-X receiver was used, which provides a bandwidth of 3.6 GHz. The data were calibrated through observations of standard bandpass (3C 84, 1055+018), phase or amplitude (1328+307, J1310+323), and flux density calibrators (LKHA101, MWC349) and reduced with the GILDAS software packages CLIC and MAP. The FWHM of the beam was 3.8 × 3.0 arcsec at 107.2 GHz, slightly larger than the SMA beamsize. The continuum and spectrum is shown in Fig. 4, with the red line indicating the expected position of the line.

No line was found at 107.2 GHz, indicating the candidate line was just a noise spike, and highlighting the difficulty in obtaining spectroscopic redshift confirmations of these faint sub-mm sources. However, we did detect the continuum emission of NGP6_D1, with a flux at $S_{107.2\,\mathrm{GHz}}$ *of* 0.56 ± 0.03 mJy, an 18.6σ detection. The derived position is at RA = 13:22:57.837 DEC = +33:24:16.61 (J2000), only 0.4 arcsec away from the pointing centre (SCUBA-2 position), and only 0.05 arcsec from the SMA position.

3 RESULTS

NGP6_D1 is detected in sub-mm, mm, and radio photometric bands, but no optical, NIR, or FIR bands. We have further determined

Downloaded from https://academic.oup.com/mnras/article/490/4/5317/5587004 by guest on 23 June 2022

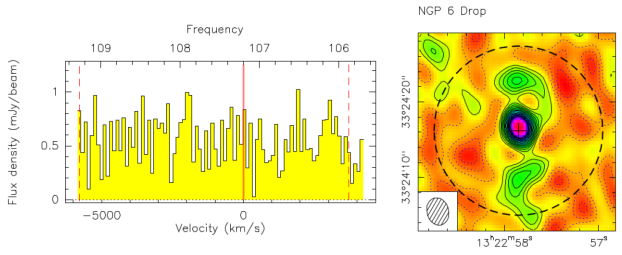


Figure 4. (Left) The NOEMA spectra surrounding the candidate line at 107.2 GHz. The solid red vertical line indicates the position of the marginal line seen in Fig. 3. (Right) The dirty map of NGP6_D1. The northern and southern side-lobes seen are artefacts from the beamshape of NOEMA, and do not represent emission. Contours are in steps of $1\sigma = 0.24$ Jy km s^{-1} beam^{-1}.

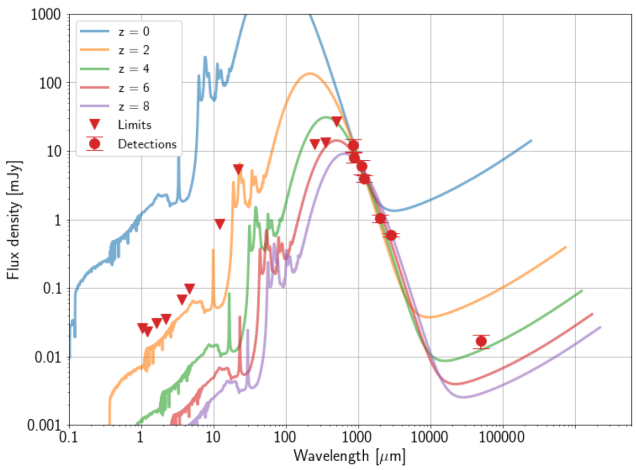


Figure 5. The ALESS average SED, as it would appear at $z = 0$, 2, 4, 6, and 8, if normalized each time to the observed 1.1 mm flux density of NGP6_D1. The red triangles shows photometric bands where we only have upper limits, whilst the points with error bars show where we have $>3\sigma$ detections.

it is likely either a single source, or very close merger, with on-sky separation of <2 arcsec. Despite this, we have been unable to determine the redshift of NGP6_D1. Well-studied local ULIRGs and SMGs are often used as templates when fitting photometric redshifts, under the assumption that the template spectral energy distribution (SED) is well matched to the underlying SED of the source (Ivison et al. 2016; Ikarashi et al. 2017; Duivenvoorden et al. 2018). Under this assumption, in Fig. 5, we plot a representative SMG SED (the ALESS average SED; da Cunha et al. 2015) at redshifts of 0, 2, 4, 6, and 8, normalizing each time to the 1.1 mm detection (arbitrarily) of NGP6_D1. We then overplot our optical or NIR limits, and observed sub-mm, mm, and radio detections. As can be seen, the lack of a SPIRE detection immediately implies very red sub-mm colours for NGP6_D1; at any redshift below $z = 4$–6, we would expect to detect NGP6_D1 in at least one of the SPIRE bands, and at $z < 2$ likely in the optical and NIR bands as well. The SPIRE photometry is consistent with NGP6_D1 being at least a 500 μm riser, if not an 850 μm riser. In this Section, we attempt to estimate a photometric redshift for NGP6_D1, and use this to derive a luminosity. Furthermore, we will examine the radio detection and CO limits, and their implications for the dust mass of NGP6_D1.

3.1 Redshift estimates

Constraining the redshift of individual FIR or sub-mm detected objects is notoriously difficult. The two most common options include fitting single modified blackbodies with and without priors (Greve et al. 2012; Riechers et al. 2013; Weiß et al. 2013; Strandet et al. 2016), and template fitting using a single or a library of templates (Lapi et al. 2011; Pearson et al. 2013; Ivison et al. 2016). Both options require a questionable set of assumptions, in the case of fitting single temperature blackbodies the assumption that a single temperature fits the true SED well (see Strandet et al. 2017 for a counterexample), and in the case of template fitting that one or any of the templates are well matched to the SED of the source. Given the SPIRE-dropouts are poorly studied in general, we cannot be certain that either of these assumptions are valid here. Furthermore, as we only have weak constraints from our *Herschel* non-detections on the most prominent feature of the FIR SED, the frequency peak of the SED, it is prudent to be conservative in our estimates of the redshift. As such, we opt to use both methods, whilst adopting broadly conservative priors and template libraries, so as to correctly reflect our ignorance.

3.1.1 Fitting templates

Whilst a single template may not accurately reflect the SED of a single source, a broad range of templates that span a larger range of parameter space will likely capture the true uncertainty in the redshift of a source. This procedure was thoroughly investigated as applied to DSFGs in Ivison et al. (2016), which demonstrated its effectiveness in recovering the redshifts of DSFGs with known spectroscopic redshifts.[2] To estimate the redshift of NGP6_D1, we utilize eight separate templates which host a broad range of properties: Cosmic Eyelash (Danielson et al. 2010; Ivison et al. 2010; Swinbank et al. 2010), ALESS average (da Cunha et al. 2015), Arp 220 (Rangwala et al. 2011), M82, NGC 6090, IRAS 20551−4250, IRAS 22491−1808, and two sources with known AGN, Mrk 231 and a QSO template. The last six of these are all from the Polletta et al. (2007) library of SEDs.

On the left of Fig. 6, we plot the best-fitting redshift and normalization for each of the eight templates. We use the photometry given in Table 1, excluding the radio point since not all templates include radio data. In each case and for each template, we minimize the χ^2 between the template and our data, allowing both the normalization amplitude and redshift to vary. This gives, for each template, a best-fitting redshift for NGP6_D1. We additionally plot the χ^2 as a function of redshift for the procedure on the right of Fig. 6, showing that each template performs similarly and additionally highlighting the reasonably broad minimum for each template. To obtain a likely redshift range, we take both the template with the lowest best-fitting redshift and the template with the highest best-fitting redshift (in this case NGP 6090 and IRAS 20551−4250, respectively), and use this range as the likely redshift range appropriate for NGP6_D1. We stress this is specifically *not* an error range, which would slightly extend this range beyond its limits, but is a range of best-fitting redshifts, given a broad range of templates from the literature.

[2]It is worth noting, however, that this assumption is not always valid, even when using numerous templates; Ikarashi et al. (2017) fit SMGs from a parent sample of 185 SED templates, and whilst able to accurately fit most of their sources, they are still unable to find a good fit for HFLS3, which they ascribe to HFLS3's warm dust temperature (sections 4.1 and 4.3 of Ikarashi et al. 2017).

Downloaded from https://academic.oup.com/mnras/article/490/4/5317/5587004 by guest on 23 June 2022

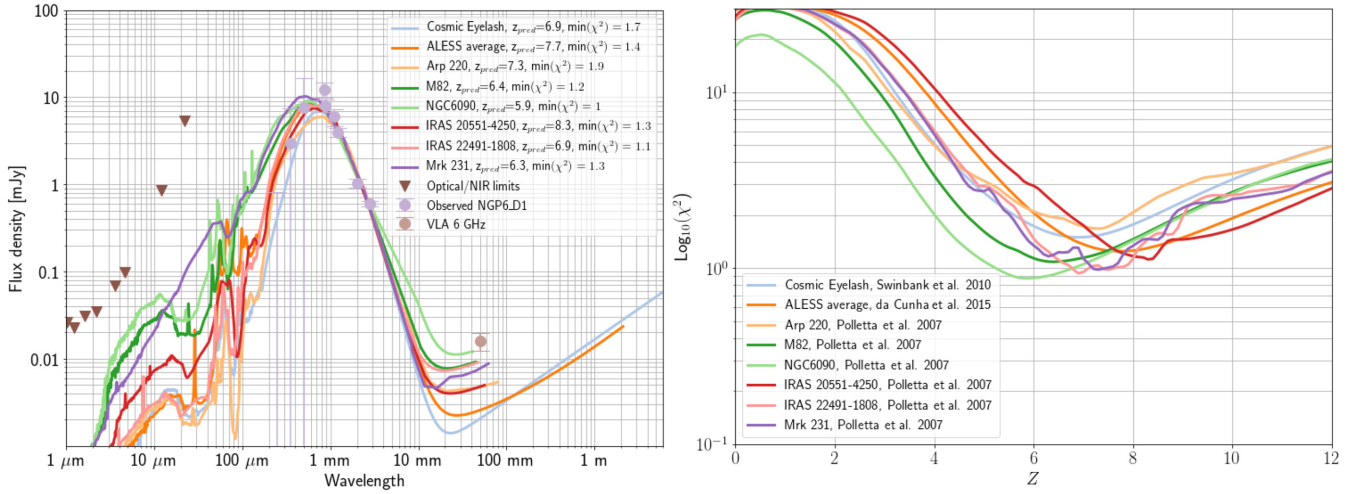


Figure 6. *Left:* The best-fitting redshift and amplitude for eight templates fit to the photometry of NGP6_D1. The solid coloured lines show the different templates, whilst the legend shows the best-fitting redshift and minimum χ^2. The grey points with error bars show the photometry used in the fits, the pink point shows the radio point not used in the fit, and the brown triangles show the optical or NIR upper limits. *Right:* The χ^2 as a function of redshift for all of the templates used in our fitting. The colours correspond to the plot on the left, and the source for each of the templates is provided in the legend.

For NGP6_D1, the best-fitting redshift ranges from a minimum of $z = 5.88$ to a maximum of $z = 8.33$, with a mean and median redshift estimate from all the templates around $z \sim 6.9$. Assuming the true redshift lies somewhere within this range, this implies that NGP6_D1 is likely one of the highest redshift DSFGs found to date. The reduced χ^2 values range between $\chi^2_\nu = 0.125$ and 0.24, indicating that in all cases we are generally overfitting the models. This is not surprising given the lack of informative features in the long wavelength tail of the dust SED; a single detection in the optical, NIR, or mid-infrared would significantly help constrain the true redshift.

However, does such a fit generally contain the true redshift of the source? To test this, we searched for all the examples we could find of $z > 3$ DSFGs with spectroscopic confirmation and similar observed photometry to NGP6_D1, and ran those sources through our template fitting procedure. We additionally selected a number of sources from the BLAST survey (Chapin et al. 2011) to test that our procedure would also correctly identify lower redshift $z < 3$ sources. In Fig. 7 we plot the results of our fitting procedure to all similar high-z sources in the literature, as well as sources from the BLAST survey. The data used for fitting in each case broadly matches those we have for NGP6_D1 (i.e. the *Herschel*-SPIRE bands plus a number of sub-mm and mm bands, where available). As can be seen, in almost all cases the true redshift is contained within the min–max range given by the fits. The only exceptions to this, excluding the BLAST sources which are generally only detected in 1–2 FIR bands, are SPT-0311-58 (Strandet et al. 2017) and LSW 20 (Dowell et al. 2014), which are under and overpredicted, respectively. The reasons for these discrepancies are not clear; both are 500 μm risers, and both have dust temperatures between ∼40 and 60 K.[3] These errors indicate the inherent difficulty in fitting photometric redshifts from templates, but it is encouraging that all the other $z > 3$ sources are well fit by our choice of templates. Nevertheless, the possibility that NGP6_D1 could be similar to LSW-20 or SPT0311-58, and possibly lie at a lower or higher redshift than predicted, cannot be discarded.

[3]It is important to note that SPT0311-58 is poorly fit by a single temperature, and indeed Strandet et al. (2017) use a two-component model, with a cold and warm dust temperature of 36 ± 7 K and 115 ± 54 K, respectively.

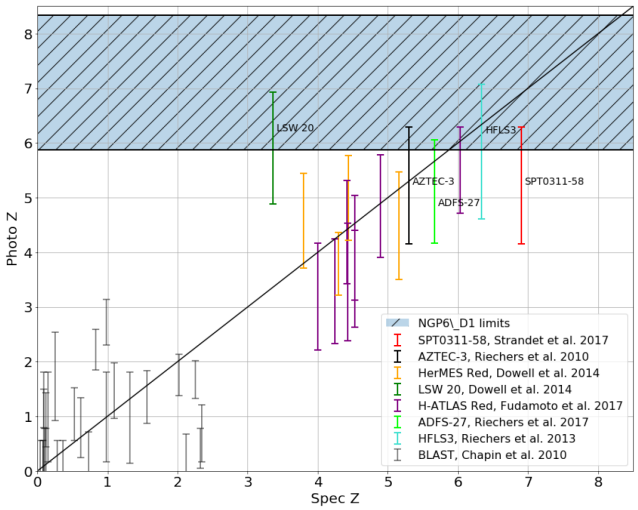


Figure 7. A comparison between the photometric and spectroscopic redshift of a variety of literature DSFGs, with photometric redshift fit using the method described in the text. Origins of the data are shown in the legend, whilst several well-known DSFGs are labelled with text to their right. The blue shaded region represents the photometric redshift estimate for NGP6_D1.

Comparing the predictions for NGP6_D1 to the other high-z literature DSFGs, it is clear that NGP6_D1 is predicted to lie at a higher redshift than all other known sources. Its low redshift estimate at $z = 5.9$ is already higher than the highest redshift estimate for all but six sources. Its high redshift estimate at $z = 8.3$ is higher than any other high redshift estimate for any other source. As detailed above, there are many uncertainties to these fits, but in general fitting to templates favours a high-z $z > 5$ solution for NGP6_D1.

However, if our source is much cooler than, or has an SED intrinsically different to, the templates used here, then our templates will be poor fits and are unlikely to correctly identify the redshift of

Downloaded from https://academic.oup.com/mnras/article/490/4/5317/5587004 by guest on 23 June 2022

the source. LSW 20 is a good example of where this fitting procedure fails (see Dowell et al. 2014, for more extensive examination of LSW 20), and if NGP6_D1 is similar to LSW 20, then we may expect NGP6_D1 to have a redshift significantly lower than predicted here. In the next Section, we therefore look to fitting single modified blackbodies to our source, which can have a broad range of temperatures and redshifts, and examine at any given redshift, what dust temperatures our source would need to posses, and whether these are physically sensible.

3.1.2 Fitting single modified blackbodies

In order to model the thermal emission from NGP6_D1, we assume the FIR spectrum is well represented by a single dust temperature modified blackbody (Blain 2002; Magnelli et al. 2012; Bianchi 2013; Casey, Narayanan & Cooray 2014). This model usually takes the form:

$$S_\nu \propto (1 - \exp(-\tau_\nu))B_\nu, \quad (1)$$

where S_ν is the observed flux density at frequency ν, $\tau_\nu = (\frac{\nu}{\nu_0})^\beta$, and gives the optical depth at frequency ν, ν_0 is the frequency at which the optical depth equals unity, and $B_\nu = B_\nu(\nu, T_{\rm dust})$ is the Planck function. β, is usually assumed to be $\beta = 1.5$–2 for SMGs (Blain 2002; Casey et al. 2014). In this model, there are five parameters to be fit: the redshift z, the average dust temperature $T_{\rm dust}$, the dust emissivity β, the frequency at which the optical depth reaches unity ν_0, and an overall normalization parameter a.

To fit our data to this model, and similar to Dowell et al. (2014) and Asboth et al. (2016), we use the affine invariant Markov Chain Monte Carlo (Goodman & Weare 2010) ensemble sampler PYTHON package, EMCEE (Foreman-Mackey et al. 2013). We use the following uninformative priors for our parameters: $0 < z \leq 12$, $T_{\rm CMB}(z) \leq T_{\rm dust} \leq 80$, $1 \leq \beta \leq 3$, $1\ \mu{\rm m} \leq c/\nu_0 \leq 1$ mm, and $-2 \leq \log_{10}(a) \leq 2$, where $T_{\rm CMB}$ gives the cosmic microwave background (CMB) temperature at redshift z, and c gives the speed of light. For numerical stability, at each sample we first normalize to the 850 μm observation, and allow the normalization a to vary from there. Tests showed the choice of normalization band did not significantly affect our final results. The redshift, normalization, and ν_0 priors are broad and chosen to ensure it is unlikely that these parameters lie outside this range; the temperature prior was chosen to ensure the dust temperature is above the CMB temperature, and generally reflects the known distribution of dust temperatures in DSFGs (Chapman et al. 2005; Casey et al. 2014; Clements et al. 2018), and the β prior is typical of what is found in the literature (Bianchi 2013; Casey et al. 2014). We ran experiments using different and more informative priors, but found that, in general, we were often reproducing our prior, justifying our choice of an uninformative prior.

To perform our fit, we use 100 walkers over 10 000 steps, throwing away the first 1000 samples in each chain as a burn-in phase and manually examining the chains to ensure that the samples have fully burnt-in. Fig. 8 shows the results of the fit, using the same photometry data in Table 1. The temperature-redshift degeneracy can clearly be seen, and indicates that, as expected, we are unable to constrain either the redshift or temperature individually (though we are able to constrain their ratio reasonable well). The ν_0 parameter generally favours $c/\nu_0 < 100$ μm, indicating that our fits are well matched by an optically thin model. Our normalization suggests that the observed SCUBA-2 flux density of NGP6_D1 is higher than its true value, in agreement with our SMA observations. The β values are lower than many other $z > 4$ sources in the literature (Riechers et al. 2013; Fudamoto et al. 2017), but within the expected range (though removing the NIKA data can raise this value, as is shown in Appendix). Additionally, in Fig. 9, we plot 3000 single modified blackbody fits to the model, with parameters chosen at random from the samples in the posterior. As expected, most of the uncertainty lies in the SPIRE bands, where our constraints are weakest.

3.2 FIR luminosity, SFR, and dust mass

We calculate the FIR luminosity by integrating between 42.5 and 122.5 μm on the resulting rest-frame FIR SED produced using the parameters from each of the 9000 samples shown in Fig. 8. We additionally calculate the dust mass for which we follow Riechers et al. (2013), and use

$$M_{\rm dust} = S_\nu D_L^2[(1+z)\kappa_\nu B_\nu(T)]^{-1}\tau_\nu[1 - \exp(-\tau_\nu)]^{-1}, \quad (2)$$

where S_ν gives the rest-frame flux density at 125 μm, D_L is the luminosity distance, κ_ν is the mass absorption coefficient, and is assumed to be $\kappa_\nu = 2.64$ m^2 kg^{-1} at 125 μm (Dunne, Eales & Edmunds 2003). In Fig. 10 we show our results. This method was also tested on photometry from HFLS3 (Riechers et al. 2013), excluding the redshift, and we found that the literature values of these parameters were generally within the 14th–86th percentiles of our predictions.

We next examine the fitted parameters and results derived from them, and compare our results for NGP6_D1 to other objects in the literature. The $T_{\rm dust}/(1+z)$ parameter of NGP6_D1 is lower than is generally seen in the 500 μm risers in table 3 of Dowell et al. (2014) and Fig. 8 of Asboth et al. (2016). These have typical values of around 9–12, with only one source, FLS 32 in Dowell et al. (2014), having a comparable $T_{\rm dust}/(1+z) = 6.7 \pm 3$. However, our result is consistent with the $z > 4$ Ivison et al. (2016) selected sources, the current spectroscopically confirmed sources of which are listed in Fudamoto et al. (2017), and have an average $T_{\rm dust}/(1+z)$ parameter of 6.05 ± 0.44, in much better agreement with our result for NGP6_D1. The spectroscopically confirmed Chapman et al. (2005) sources have temperatures fit using single temperature modified blackbodies, though with a fixed β value of $\beta = 1.5$. They find a mean $T_{\rm dust}/(1+z)$ of 12.3 ± 3.0, once again significantly higher than we have found for NGP6_D1, with no sources where $T_{\rm dust}/(1+z) < 8$. The redshift distribution of their sources is also limited to $z < 4$, with most of their sources at $2 < z < 3$. The predicted FIR luminosity of NGP6_D1 is reasonably well constrained, with $\log_{10}(L_{\rm FIR}) = 12.70^{+0.21}_{-0.78}$, where the errors give the 14th and 86th percentiles of the posterior distribution. These values suggest NGP6_D1 is likely a ULIRG, and if it is at $z > 4$ as our observations suggest, it is likely one of the least luminous detected $z > 4$ DSFGs to date (see table 7 of Fudamoto et al. 2017 for a comparison of several literature $z > 4$ DSFGs and their derived properties). It may be more representative of the general $z > 4$ DSFG population. We convert this FIR luminosity to an SFR by using equation (4) of Kennicutt (1998), and convert to a Kroupa IMF by dividing by 1.5, as described in Schiminovich et al. (2007; see also Hayward et al. 2014). This gives

$${\rm SFR}[{\rm M}_\odot\ {\rm yr}^{-1}] = 1 \times 10^{-10} L_{\rm FIR}\ [{\rm L}_\odot], \quad (3)$$

which leads to a predicted SFR for NGP6_D1 of 512^{+301}_{-426} M$_\odot$ yr^{-1}. This value is an order of magnitude lower than almost all other non-lensed $z > 4$ DSFGs (see table 7 of Fudamoto et al. 2017), with the notable exception of HDF 850.1 (Walter et al. 2012), which has an SFR corrected for lensing (using the magnification estimated by Neri et al. 2014) of $\sim$530 M$_\odot$ yr^{-1}. We find this result

Downloaded from https://academic.oup.com/mnras/article/490/4/5317/5587004 by guest on 23 June 2022

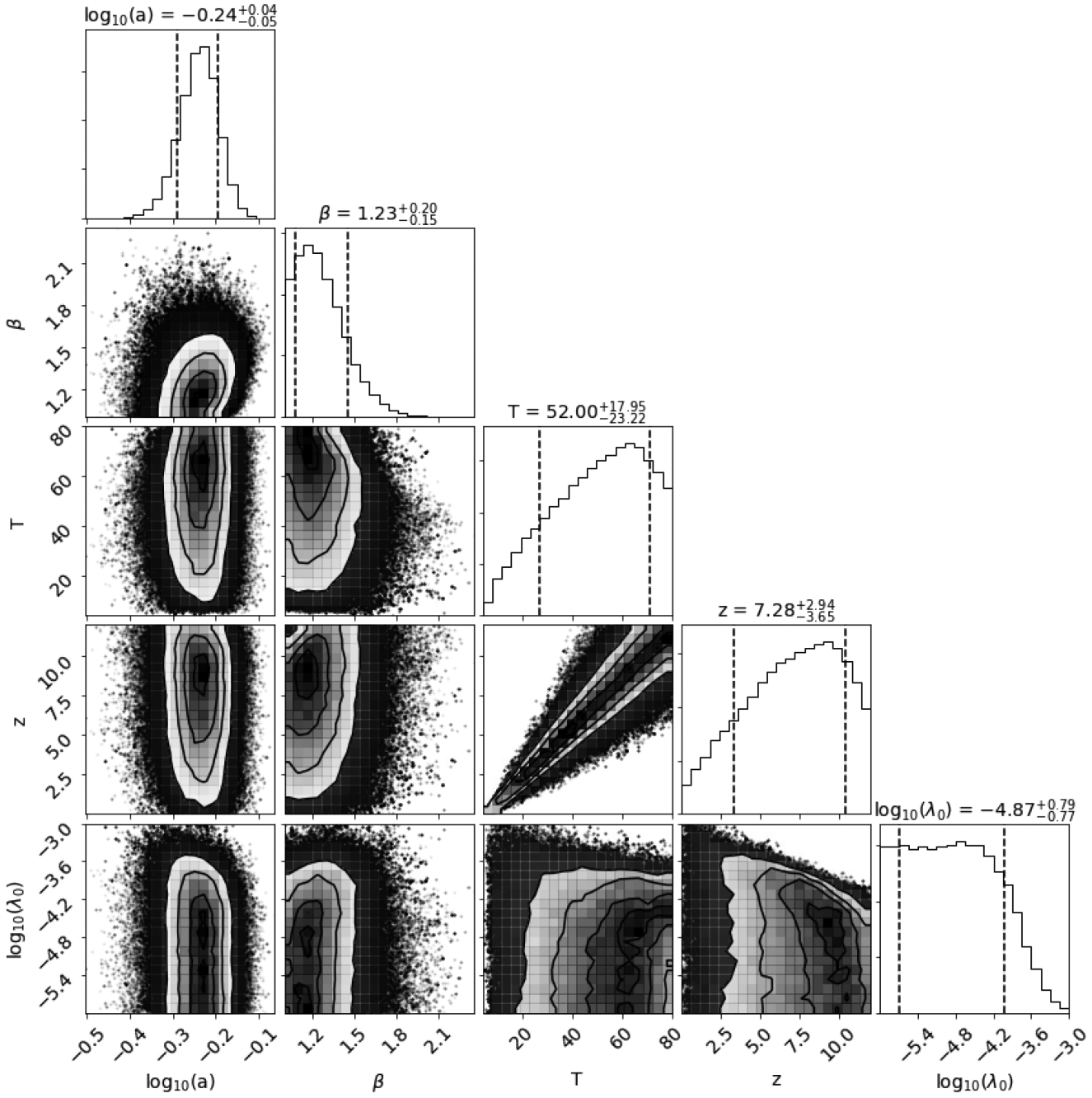


Figure 8. The samples and marginalized posteriors obtained after fitting the model described in equation (1) to the photometry from NGP6_D1. Median values are given above each parameter, whilst errors are taken from the 14th and 86th percentile of each marginalized posterior. The vertical dashed lines also show the 14th and 86th percentiles.

notable, because HDF 850.1 is also the only other SPIRE dropout in table 7 of Fudamoto et al. (2017), indicating that SPIRE-dropouts may represent the more populous lower luminosity DSFGs at $z \geq 4$.

The predicted dust mass for NGP6_D1 is between 10^8 and 10^9 $M_\odot$, slightly lower than, but comparable to, other literature values (table 6 of Fudamoto et al. 2017). Of the six dust masses presented by Fudamoto et al. (2017), only one (G09-83808c) is as low as the predicted value for NGP6_D1, and this one source is additionally gravitationally lensed by a factor of 8.2 ± 0.3 (Oteo et al. in prep).

3.3 CO lines, CO luminosity, and gas mass

Our spectroscopic observations from both EMIR and the RSR generally cover from 73 to 114 GHz to a similar RMS of around 0.5–0.7 mJy. We estimated the expected CO line flux densities for NGP6_D1 by multiplying the observed 850 μm flux density of NGP6_D1 by the CO line flux to 850 μm continuum ratio in several other high-redshift DSFGs. In Fig. 11, we plot these estimates for six well-studied DSFGs, as well as the detection limits of our EMIR and RSR observations. As our detection limit is dependent on the assumed rotational velocity of NGP6_D1 (which determines to what

Downloaded from https://academic.oup.com/mnras/article/490/4/5317/5587004 by guest on 23 June 2022

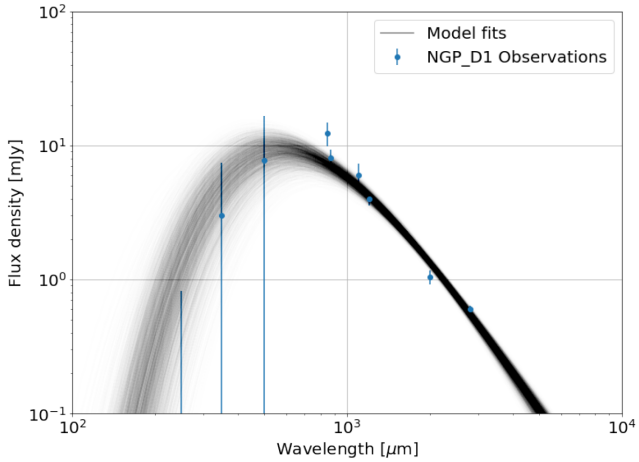


Figure 9. 3000 randomly chosen model fits from Fig. 8, compared to observations of NGP6_D1.

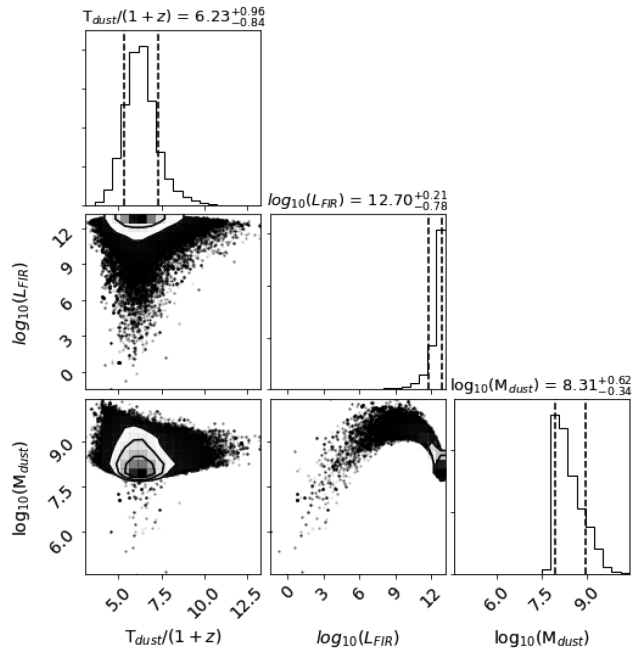


Figure 10. Derived parameters for NGP6_D1, using the samples from Fig. 8.

velocity we smooth our data), we plot an estimate for both 100 and 500 km s^{-1} with the later being typical for high-z DSFGs (Bothwell et al. 2013; Fudamoto et al. 2017).

At the redshifts estimated from template fitting, between 72 and 114 GHz, we expect to see the CO(5-4)-CO(8-7) transitions. These are typically the brightest CO lines seen in DSFGs (see Fig. 11). Given no detection, we place 3σ upper limits of 2.4 mJy at a resolution of 100 km s^{-1} and 1.5 mJy at a resolution of 500 km s^{-1}. Fig. 11 suggests we can rule out a CO line flux in NGP6_D1 that is similar to AZTEC3 (Riechers et al. 2010) or HDF 850.1 (Walter et al. 2012). We may be able to marginally rule out a line flux similar to ADFS-27 (Riechers et al. 2017), under the assumption that the line widths in NGP6_D1 are ∼500 km s^{-1}. We cannot, however, rule out a spectral line energy distribution (SLED) similar to HLSJ09 (Combes et al. 2012) or HFLS3 (Riechers et al.

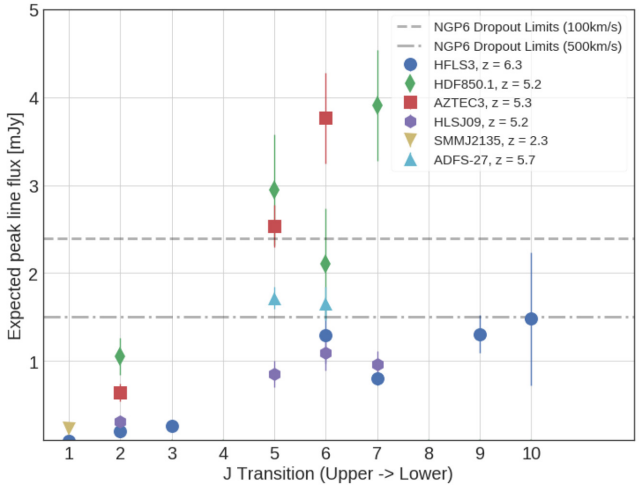


Figure 11. The expected peak line flux of the CO line transitions of NGP6_D1, as estimated from several well-studied high-z DSFGs and indicated using the different coloured markers. Each marker represents the peak line flux for that DSFG and at that J transition. The dashed line shows the upper limits at 100 km s^{-1}, whilst the dot–dashed line shows the upper limits at 500 km s^{-1}.

2013). Our observations therefore approach limits that suggest that NGP6_D1 might be CO deficient compared to other high-z DSFGs.

We also place our CO luminosity upper limit on the observed $L'_{CO(1-0)}$– L_{FIR} correlation for galaxies with high star-formation efficiencies. We follow equations (6) and (7) from Bothwell et al. (2013) to estimate CO luminosity upper limits using the RMS noise per 31 MHz channel of the RSR spectrum, a mean linewidth of 500 km s^{-1} (typically expected for DSFGs) and adopting several redshift solutions from 0 to 10. Fig. 12 shows the $L'_{CO(1-0)}$– L_{FIR} correlation for (U)LIRGs ($z \leq 0.1$) and DSFGs ($z \geq 1$) from the literature at different redshifts.

In Fig. 12 we plot our CO luminosity upper limit for a $z = 4$ solution represented by the yellow triangle at the FIR luminosity obtained in Section 3.2. For higher z solutions, the upper limit moves towards the right (e.g. see black triangle for $z = 8$ upper limit). It is worth noting that $4 < z < 8$ solutions are well located within the scatter of the correlation of the ULIRG luminosity regime, as expected. Despite only a handful of $z > 4$ DSFGs being located within the ULIRG regime on the $L'_{CO(1-0)}$– L_{FIR} diagram, NGP6_D1's upper limits suggest that this source could have similar properties to other $z > 4$ DSFGs, like ALESS65.1 ($z = 4.4$; Huynh et al. 2017), AzTEC/C159 ($z = 4.6$; Jiménez-Andrade et al. 2018), HDF850.1 ($z = 5.2$; Walter et al. 2012), SDSSJ1044–0125 ($z = 5.8$; Wang et al. 2013), and G0983808 ($z = 6.0$; Zavala et al. 2018).

If NGP6_D1 lies at $z < 4$, a CO detection would be expected, though the scatter in Fig. 12 means that a non-detection in our current data set remains a possibility. Deeper spectroscopy of this source, with LMT@50 m, for instance, would exclude this possibility.

Our upper limits at $z > 4$ lead to a molecular gas mass upper limit for NGP6_D1 of $\sim 1 \times 10^{11}$ M$_\odot$ and a upper limit to the gas depletion time, $\tau_{dep} = M_{H2}/SFR$ of ∼800 Myr, which encompasses the ∼100 Myr depletion times seen in DSFGs and barely rejects ∼1 Gyr depletion times seen in normal[4] $z > 1$ galaxies (Tacconi et al. 2010; Bothwell et al. 2013; Carilli & Walter 2013).

[4]i.e. not mergers or quasars, which are more typically studied at $z > 1$.

Downloaded from https://academic.oup.com/mnras/article/490/4/5317/5587004 by guest on 23 June 2022

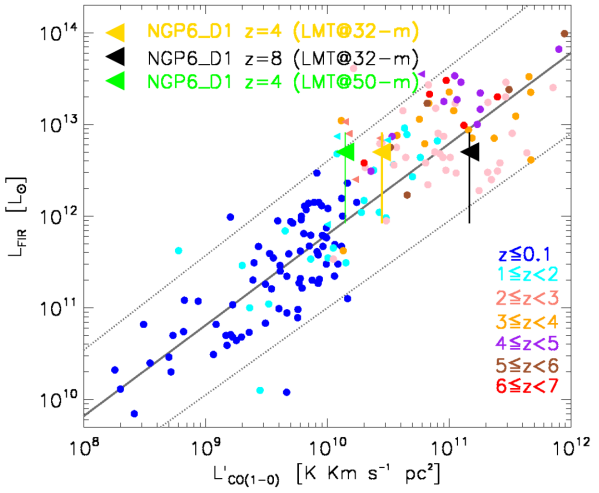


Figure 12. $L'_{CO(1-0)}$– L_{FIR} correlation for (U)LIRGs ($z \leq 0.1$; Papadopoulos et al. 2012) and DSFGs ($z \geq 1$, Riechers et al. 2010; Harris et al. 2012; Bothwell et al. 2013; Yun et al. 2015; Aravena et al. 2016; Riechers et al.2017; Strandet et al. 2017; Yang et al. 2017; Zavala et al. 2018; Gullberg et al. 2018; Jiménez-Andrade et al. 2018) from the literature at different redshifts (coloured circles and legends). Overplotted is the parametrized $L'_{CO(1-0)}$– L_{FIR} relation proposed by Greve et al. (2014; grey solid line) with the associated scatter of the data (grey dotted lines). We show our CO luminosity upper limits for $z = 4$ and $z = 8$ solution represented by the yellow and black triangles, respectively, with vertical error bars of the size of FIR luminosity uncertainty obtained in Section 3.2. We also show the same $z = 4$ solution for a non-detection, but observed with RSR at LMT@50 m (green triangle), which will be near twice the depth of our current RSR observations at LMT@32 m.

4 DISCUSSION

4.1 Comparison to the literature

In this Section, we compare NGP6_D1 to other dropout-like sources in the literature. Only recently have large surveys at 850 μm been completed, so few examples of 850 μm risers or SPIRE dropouts have been published to date.

Ikarashi et al. (2017) identify and characterize two sources, selected partially on the basis of their faint SPIRE emission. These sources are undetected in SPIRE, but are both detected by SCUBA-2 at 850 μm and ALMA at 1.1 mm, with flux densities of ∼4.5 and ∼3.0 mJy each in the respective bands. One source, ASXDF1100.053.1, is further detected by the VLA at 6 GHz, with a flux density of 4.5 ± 1.1 μJy. Compared to NGP6_D1, these sources are 4 times fainter at 850 μm, despite neither NGP6_D1 nor either of the Ikarashi et al. (2017) sources being detected in SPIRE. Furthermore, NGP6_D1 is 4 times brighter at 6 GHz compared to ASXDF1100.053.1.

Boone et al. (2013) found a SPIRE-dropout during APEX and Laboca follow up in the *Herschel* Lensing Survey (Egami et al. 2010). They conclude that it is possibly a low-luminosity source ($L_{FIR} < 10^{12}$ $L_\odot$) at z > 4 that is being lensed, possibly multiple times, by the brightest cluster galaxy in AS1063 (RXC J2248.7-4431). They further postulate this dropout source may be associated with an optically detected z = 6.107 system. Further follow-up work by Boone et al. (2015) reveals numerous dropout sources amongst the *Herschel* Lensing Survey fields, with ALMA and NOEMA programs underway to determine the nature of these sources. The key difference between NGP6_D1 and the dropouts found in the *Herschel* Lensing Surveys is that there is no evidence that NGP6_D1 is being lensed by any structure.

ADFS-27 is a dusty major merger and an 850 μm riser ($S_{850} > S_{500} > S_{350}$) at $z = 5.655$ (Riechers et al. 2017). As ADFS-27 has its observed SED peak at ∼850 μm, a lower luminosity variant would likely still be detected by SCUBA-2, but remain undetected by SPIRE. A fainter version of ADFS-27 would thus be classed as a SPIRE dropout, similar to NGP6_D1.

4.2 What are the SPIRE dropouts?

Given what we have learned about NGP6_D1, we here examine other populations that may be similar.

The 850 μm risers ($S_{250} < S_{350} < S_{500} < S_{850}$ – often just the last of these is used due to non-detection in the shorter wavelength SPIRE bands) may represent a population of DSFGs at redshifts $z > 6$ (Ikarashi et al. 2017; Riechers et al. 2017). The idea behind this is similar to the 500 μm riser population (Dowell et al. 2014; Asboth et al. 2016; Ivison et al. 2016), at $z \geq 6$ the rest-frame ∼100 μm peak of dust emission would be redshifted into the 850 μm band. A source bright enough to be detected at both 850 and 500 μm would then be classed as an 850 μm riser. This population potentially relates to NGP6_D1; a source with a 500 μm flux density below the nominal SPIRE detection threshold, but still detected at 850 μm would be classed as a SPIRE dropout.

Few confirmed 850 μm risers are known. As part of a follow up of 500 μm risers, Riechers et al. (2017) discovered ADFS-27, a binary HLIRG 850 μm riser. It has a spectroscopically confirmed redshift of $z = 5.655$ and a luminosity of 2.4×10^{13} $L_\odot$. Despite this high luminosity, ADFS-27 is only just bright enough to be detected in the SPIRE bands in the deepest *Herschel* surveys (Riechers et al. 2017). These authors suggest that the surface density of 850 μm risers could be as low as 9×10^{-3} deg^{-2}, if ADFS-27 remains the only 850 μm riser amongst the SPIRE-only detected 500 μm risers. The rarity of 850 μm risers is supported by Ivison et al. (2016), who followed up a sample of 109 red SPIRE sources from the H-ATLAS survey with SCUBA-2, and found no 850 μm risers.

A key difference between the Ivison et al. (2016) sample and ADFS-27, however, is the flux density at 500 μm; whilst the Ivison et al. (2016) sample had a minimum 500 μm flux density of 30 mJy from completeness considerations, the 500 μm flux of ADFS-27 is only 24.0 ± 2.7 mJy. Indeed, HDF-850.1 (Walter et al. 2012), the only other well-studied SPIRE dropout, is undetected in SPIRE, with a 500 μm flux density <21 mJy. What luminosity would a typical DSFG have to have in order to be detected in SPIRE at ($S_{500} > 30$ mJy), and be an 850 μm riser ($S_{850} > S_{500}$)? In the top panel of Fig. 13, we plot the luminosity, redshift, and dust temperature a source would need to be detected in both SPIRE at 500 μm and SCUBA-2 at 850 μm, whilst also having $S_{850} > S_{500}$. We would not expect to see many 850 μm risers at $z < 4$, as they would require cold dust temperatures of <30 K. Using equation (2) these requirements would lead to dust masses $>10^{10}$ $M_\odot$, 2 orders of magnitude higher than seen typically in the literature (da Cunha et al. 2015). At $z > 5$, however, we would also expect sources to be rare, as only the most luminous HLIRG and above systems with dust temperatures of 40–50 K would be detected as 850 μm risers. These results seem to contrast with the observed $T_{dust}/(1+z)$ of ADFS-27, with $T_{dust}/(1+z) = 8.3$ at $z = 5.655$. However, it should be noted that ADFS-27 is a merger of two systems, with a separation of around 10 kpc. Even though they are at the same redshift, it is possible to construct a viable 850 μm riser SED; experiments show that fitting dual single modified black bodies to the two components of ADFS-27, with

Downloaded from https://academic.oup.com/mnras/article/490/4/5317/5587004 by guest on 23 June 2022

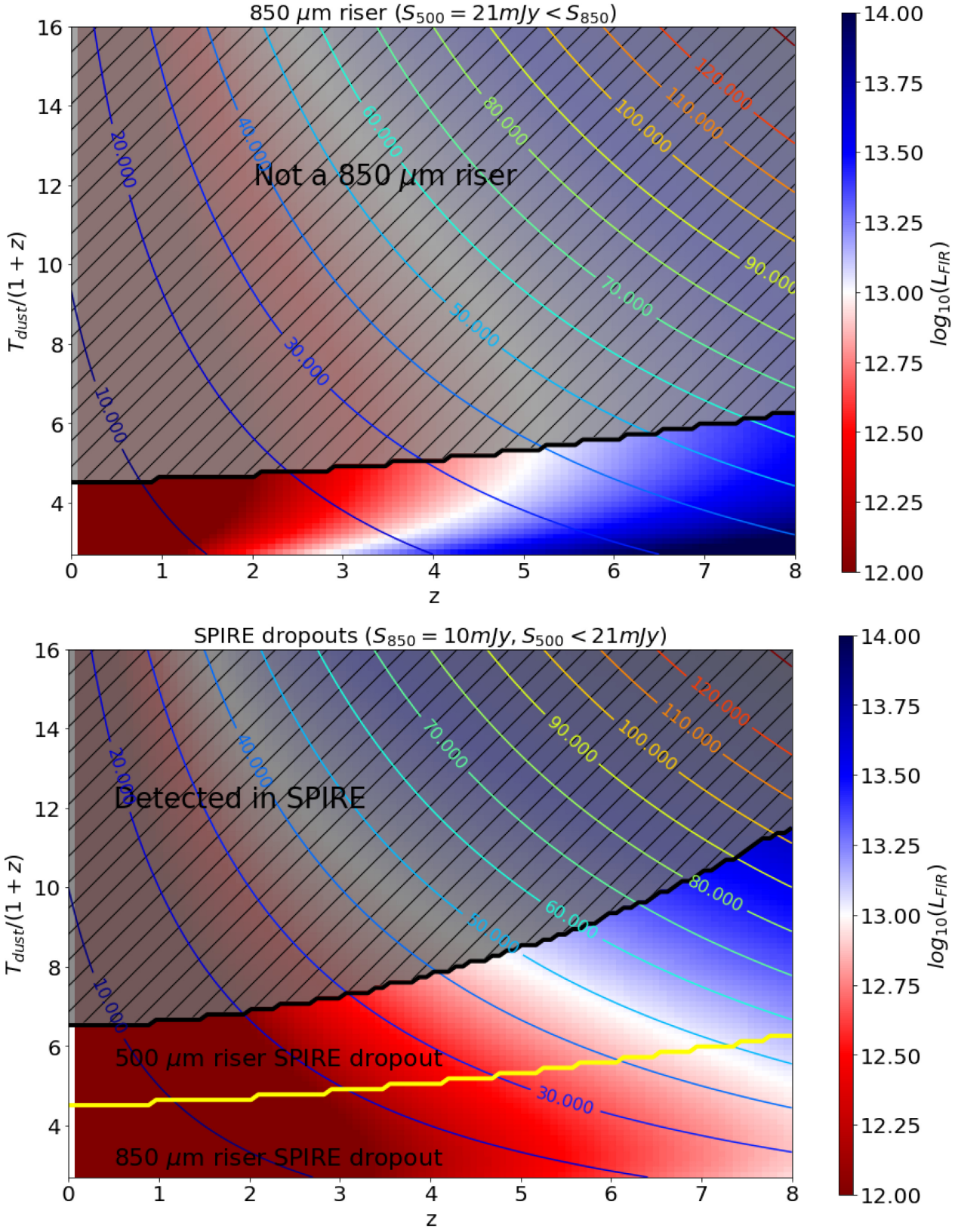


Figure 13. *(Top)*: $T_{\rm dust}/(1+z)$ against z for a single modified blackbody with $\beta = 2.$ and $\nu_0 = 100$ μm, normalized to $S_{500} = 21$ mJy. The shaded region shows where this source is *not* an 850 μm riser, whilst the background colours show the luminosity of such a source as a function of z and $T_{\rm dust}$. *(Bottom)*: The same as the top, but for a SPIRE dropout with normalization $S_{850} = 10$ mJy. The shaded region shows where the source is *not* a SPIRE dropout, whilst the yellow line separates out SPIRE dropouts which are also 500 μm risers from those which are 850 μm risers. The lower y limit is constrained by the CMB temperature as $y = 2.73 \times (1+z)$, whilst the upper is chosen to broadly fit sources from the literature.

Downloaded from https://academic.oup.com/mnras/article/490/4/5317/5587004 by guest on 23 June 2022

~20 and ~50 K dust temperatures, can accurately reproduce the observed SED of the dual system.

The SPIRE dropouts may also be fainter analogues of the 500 μm risers; a 500 μm riser too faint to be detected in the SPIRE bands may still be detected at 850 μm due to the different depths SPIRE and typical 850 μm instruments reach. Indeed, given the depths reached in our observations, it is entirely plausible that NGP6_D1 is merely a 500 μm riser as opposed to an 850 μm riser. In the bottom panel of Fig. 13, we plot a SPIRE dropout with an 850 μm flux density of 10 mJy. We further indicate where, in the plot of $T_{\rm dust}/(1+z)$ versus z, such a source would be detected in SPIRE (and therefore not be a dropout), where it is a fainter version of a 500 μm riser, and where it is a fainter version of an 850 μm riser. For a source with an 850 μm flux density of 10 mJy, about half of the parameter space would not be detected in SPIRE, including ULIRGS with $z \gtrsim 4$ and/or $T_{\rm dust} < 50$ K sources.

Comparing the two panels of Fig. 13, it is immediately apparent that the SPIRE dropouts cover a much larger range of parameter space compared to the 850 μm risers seen in the top panel. Furthermore, this selection is better at sampling the lower luminosity population; it is able to select sub-HLIRG objects with dust temperatures of 30–50 K, as seen, for example, in the population studied by Chapman et al. (2005) and Miettinen et al. (2017). The SPIRE detected 850 μm risers on the other hand are limited to HLIRG-like objects at $z > 5$, and below $z = 4$ are limited to cold $T_{\rm dust} < 30$ K objects. If the trends seen at $z = 2$–3 in Chapman et al. (2005) and Miettinen et al. (2017), that *most* SMGs have dust temperatures ~30–50 K, continues to $z > 4$, then the SPIRE dropouts could well represent a population of medium dust temperature ($T_{\rm dust} = 30$–50 K), ULIRG-like objects at $z > 4$. For all reasonable luminosity functions, these sources will be more numerous than the high-luminosity HLIRGs. This kind of source would be inaccessible in the optical or NIR without the benefit of negative *k*-correction, and be inaccessible to SPIRE because of the faint emission in the observed-frame FIR.

4.3 The nature of NGP6_D1

We now return to the central question of this paper, what kind of object is NGP6_D1? It is difficult to say with certainty; whilst labelling NGP6_D1 and the SPIRE dropouts, in general, as a likely population of $z > 6$ DSFGs is attractive and a viable possibility, it is also possible that NGP6_D1 and the SPIRE dropouts are examples of a cooler, 30–50 K population of DSFGs that exist at $z = 3$–6. It is unlikely that SPIRE alone can be of much help in accessing the $z > 5$ population of DSFGs, as Fig. 13 clearly demonstrates that it cannot detect many sub-HLIRG objects at $z > 5$, unless they are lensed.

We now examine the possible nature of NGP6_D1, and attempt to rule out the least likely scenarios.

(1) Galactic. We do not detect NGP6_D1 in the optical or NIR down to AB magnitudes of 22–19. Under the assumption that our source is at $z = 0$, the FIR SED constrains the dust temperature of our source to be <10 K (see Fig. 8), and our observations from NOEMA and the SMA constrain the size of the source to be <1 light-year if NGP6_D1 is within 30 kpc of the Earth. NGP6_D1 could therefore be a giant molecular cloud (GMC), but this is unlikely for the following reasons. NGP6_D1 was detected in the northern galactic pole, where we do not expect significant contamination from galactic sources or from the disc of the Milky Way. Its temperature would be comparable to, or lower than, the cores of GMCs (Schneider et al. 2014), and sources do exist with temperatures lower than the CMB, such as the Boomerang nebula (Sahai & Nyman 1997). However, unless NGP6_D1 is at a distance of 30kpc, its size is smaller than that of other molecular clouds, which are typically around 1 light-year across (Murray 2010). A system this cold and small would be very short lived. This, combined with the lack of any extended structure around NGP6_D1, and the lack of a detection in *WISE* or *IRAS* indicate that a galactic origin is unlikely.

(2) Intermediate redshifts ($z = 0$–4). In their examination of 73 850 μm selected sources, Chapman et al. (2005) discover only nine sources with $T_{\rm dust} < 20$ K, all of which lie at z < 1. Cortese et al. (2014) also find many local (<30 Mpc) sources with dust temperatures between 10 and 20 K, but no source with $T_{\rm dust} <$ 10 K. If our source is a local ($z < 1$) galaxy, it would be one of the coldest galaxies in the Universe, with dust temperatures comparable to the CMB. Even between $z = 0$ and 4, the CMB varies in temperature between 2.7 and 13.5 K. Over the same redshift range, the temperature corresponding to the minimum χ^2 for NGP6_D1 varies between ~2.5 and 22.5 K. While the simple SED fits in Fig. 8 indicate that a $z = 0$–4 solution is possible, consideration of the CMB temperature floor makes at least the lower half of this range highly implausible. The more physical template fitting method of Fig. 6 favours a high-redshift solution, as do the existing results on similarly selected objects (Riechers et al. 2013; Dowell et al. 2014; Ivison et al. 2016; Fudamoto et al. 2017). A z ~ 2 solution thus seems unlikely.

Perhaps the most interesting possibility for an intermediate redshift solution is that NGP6_D1 is similar to LSW 20, the 500 μm riser at a redshift of only $z = 3.3$ (Dowell et al. 2014). If such sources are common, they are not accounted for in existing template libraries but will still appear among red selected samples. If this is the case, it would go some way to explaining discrepancies found when inferring general trends about the very red *Herschel*-SPIRE population, such as the overabundance of red sources (Dowell et al. 2014; Asboth et al. 2016; Béthermin et al. 2017).

(3) High redshift ($z = 4$–8). A $4 < z < 8$ solution would result in a dust temperature between 20 and 60 K, comparable to other high-z DSFGs. Template fits from other well studied sources favour this solution, generally preferring the $z > 6$ solutions over $z < 6$. The CO J(5-4), J(6-5), J(7-6), and J(8-7) lines should be visible in our spectrum, but as Fig. 11 shows, our RMS is not low enough that we can guarantee we should detect a line if our source is similar to HFLS3 or HLSJ09. We thus conclude that a high-redshift solution is the most likely explanation of NGP6_D1. Given the higher than expected radio flux (see Fig. 6), and the fact that we do not detect any CO lines, we further suggest that NGP6_D1 hosts an AGN, probably dust enshrouded, which contributes to the radio flux.

4.4 The SPIRE dropout population

Fig. 13 suggests that SPIRE dropouts can inhabit a much larger range of luminosity–redshift–temperature parameter space than 850 μm risers; the polygon that forms from the constraints that $20 < T_{\rm dust} < 80$ K, and the approximate 'knee' of the $z > 2$ DSFG luminosity function[5] at around 10^{13} $L_\odot$ (Casey et al. 2014; Gruppioni et al. 2017; Koprowski et al. 2017) encompasses a much larger area of parameter space for the SPIRE dropouts compared to the 850

[5]No 850 μm riser nor SPIRE dropout has a dust temperature above 20 K below this redshift.

Downloaded from https://academic.oup.com/mnras/article/490/4/5317/5587004 by guest on 23 June 2022

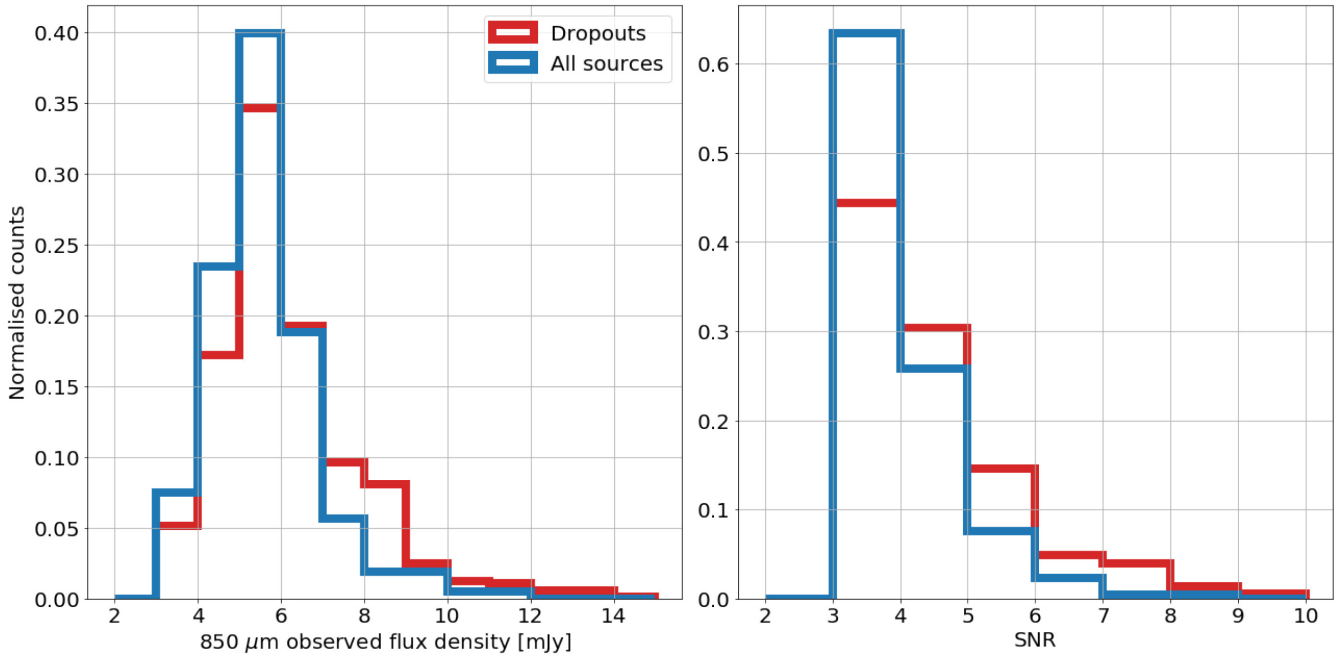


Figure 14. *Left:* The number counts of all detected SCUBA-2 sources in S2COSMOS (blue solid line), and dropouts (red solid line) corrected for boosting. Bins have widths of 1 mJy. *Right:* The SNR for the detections of all detected S2COSMOS sources and dropouts.

μm risers. We therefore examine two of the largest extragalactic surveys at 850 μm with significant *Herschel*-SPIRE survey overlap, to determine the number of SPIRE dropouts per deg^2.

Initially, we searched for dropouts among the maps and catalogues from the observed $\sim$2 deg^2 COSMOS field of the SCUBA-2 Cosmology Legacy Survey S2CLS (Geach et al. 2017), using their first data release, which reached a uniform 1σ rms error of 1.6 mJy across 2 deg^2 in the COSMOS field. The S2COSMOS catalogues require a 3.5σ detection for a source to be included in the catalogues, with a typical 1σ value of 1.09 $\pm$ 0.24 mJy at 850 μm. We then matched these catalogues to catalogues from *Herschel* to search for any dropouts among the 719 detected SCUBA-2 objects. For the *Herschel* catalogues, we used the HerMES (Oliver et al. 2012) DR2 single-band catalogues, where fluxes are extracted by the HerMES XID code (Roseboom et al. 2010; Hurley et al. 2016) at positions found by the STARFINDER code (Diolaiti et al. 2000) at the corresponding wavelength. We further assume Gaussian shaped beam FWHMs of 18.15, 25.15, and 36.3 arcsec at 250, 350, and 500 μm, respectively. No attempt is made at cross-matching between bands, and three separate catalogues are made for the three SPIRE bands individually. Using a search radius of 13.0 arcsec, equivalent to the beamsize of SCUBA-2, we cross-match the S2COSMOS sources with each of the three *Herschel*-SPIRE catalogues. We find 213 sources which have no *Herschel* match in any of the three bands, a dropout fraction of 21.8 per cent. If we use the beamsize from the *Herschel* 500 μm band of 35.2 arcsec, we still find 57 dropouts (7.9 per cent). Regardless of the precise beamsize, we find that a significant number of SCUBA-2 sources are dropouts. In Fig. 14 we examine both the normalized and deboosted flux density distribution and normalized SNR distribution of the dropout sources when using the 13 arcsec search radius and compare this to the general SCUBA-2 population. We find that the flux distributions of the dropouts and of the general population are broadly similar, with median values of 5.6 and 5.8 mJy, respectively, standard deviations of 1.3 and 1.8 mJy, and a long tail stretching towards higher flux densities. This suggests that the dropouts are not merely the faint population of 850 μm detected sources, but are a unique population of SMGs that remain undetected by *Herschel*. Examining the SNR distribution, we find that 63 per cent of dropouts have a low SNR (with detection SNR <4), compared to the general population, which has 44 per cent in this range. This may imply that a number of the dropouts are noise spikes, but 11 per cent have an SNR $>$ 5 and, as we have shown here, at least some of the dropout population consists of real sources (26 per cent of all the S2CLS sources have a detection SNR $>$5). We detect 10 dropouts with flux densities at 850 μm $>$ 8 mJy over $\sim$2 deg^2, corresponding to a source density of 5 $\pm$ 1.58 sources deg^{-2}, comparable to the 3.3 $\pm$ 0.8 bright red (S500 $>$ 30 mJy) 500 μm riser sources found by Dowell et al. (2014).

These results are confirmed by Aguilar et al. (in preparation), who make a comparison between AzTEC detected sources (i.e. S/N $>$ 3.5 at 1.1 mm) that were selected as 500 μm risers or SPIRE dropouts on three well observed blank fields: GOODS-S, GOODS-N, and COSMOS (270 sources on $\sim$0.86 deg^2 in total). They found that 20 per cent of AzTEC sources were 500 μm risers, while $\sim$30 per cent were classed as SPIRE dropouts, similar to our results in S2CLS. After identification through radio-IRAC-CANDELS counterpart analysis and sub-mm SED fitting, they suggest that more than 50 per cent of this population is at z $>$ 4. These results are in excellent agreement with our examination of S2COSMOS, and the predictions in Fig. 13. The large numbers suggest these surveys are detecting more 'normal' DSFGs at $z >$ 4, compared to the extreme sources detected by SPIRE (Riechers et al. 2013; Dowell et al. 2014; Riechers et al. 2017; Strandet et al. 2017; Zavala et al. 2018)

Downloaded from https://academic.oup.com/mnras/article/490/4/5317/5587004 by guest on 23 June 2022

5 CONCLUSIONS

NGP6_D1 is a serendipitously detected SPIRE dropout, strongly detected at $\lambda \geq 850\ \mu$m, but not detected in any shorter wavelength bands. Interferometric observations confirm it to be a single source, with no evidence for any optical or NIR emission, or nearby potential lensing sources. No $>3\sigma$ detected lines are seen in the spectrum of NGP6_D1 across 32 GHz of bandwidth, and the redshift remains unknown. CO luminosity limits were calculated and these are consistent with the $L_{\rm CO}$–$L_{\rm IR}$ correlation of other $z > 4$ DSFGs. The degeneracy between the temperature and redshift of NGP6_D1 prevents us from constraining either of these parameters strongly, but the luminosity and dust mass are reasonably well constrained, and suggest NGP6_D1 is a ULIRG-like object, with a dust mass $\sim 10^8$–10^9 M$_\odot$ and an SFR of $\sim$500 M$_\odot$ yr^{-1}. Template fitting over a range of galaxy types suggests the redshift of NGP6_D1 is most likely between $z = 5.8$ and 8.3. The upper limit on the gas mass of NGP6_D1 suggests a maximum of $M_{H2} < (1.1 \pm 3.5) \times 10^{11}$ M$_\odot$, consistent with a gas-to-dust ratio of $\sim$ 100–1000.

We also find that SPIRE dropouts account for $\sim$ 20 per cent of all SCUBA-2 detected sources, but have similar flux density distributions to the general population. We find that such dropouts likely represent either ULIRG like objects at $z > 4$, with dust temperatures around 30–50 K, comparable to those seen at $z =$ 2–3, *or* a population of $z > 6$ sources that have so far remained inaccessible to SPIRE. These results are consistent with HDF 850.1 (Walter et al. 2012), one of the few well-studied SPIRE dropouts, as well as the SPIRE dropouts identified by Ikarashi et al. (2017), though the latter sources lack spectroscopic redshifts.

ACKNOWLEDGEMENTS

The authors wish to recognize and acknowledge the very significant cultural role and reverence that the summit of Mauna Kea has always had within the indigenous Hawaiian community. We are most fortunate to have the opportunity to conduct observations from this mountain. The *Herschel*-ATLAS is a project with *Herschel*, which is an ESA space observatory with science instruments provided by European-led Principal Investigator consortia and with important participation from NASA. The H-ATLAS website is http://www.h-atlas.org/. The Submillimeter Array is a joint project between the Smithsonian Astrophysical Observatory and the Academia Sinica Institute of Astronomy and Astrophysics and is funded by the Smithsonian Institution and the Academia Sinica. This work is based on observations carried out under project number 199-15, E16AD, and 227-14 with the IRAM NOEMA Interferometer [30 m telescope]. IRAM is supported by INSU/CNRS (France), MPG (Germany), and IGN (Spain). This research made use of Astropy, a community-developed core PYTHON package for Astronomy (The Astropy Collaboration 2013). This work made extensive use of the Starlink Table or VOTable Processing Software, TOPCAT (Taylor 2005). This publication makes use of data products from the Wide-field Infrared Survey Explorer, which is a joint project of the University of California, Los Angeles, and the Jet Propulsion Laboratory or California Institute of Technology, funded by the National Aeronautics and Space Administration. This research has made use of NASA's Astrophysics Data System Bibliographic Services. This work made use of GILDAS http://www.iram.fr/IRAMFR/GILDAS, a collection of state-of-the-art software oriented toward (sub-)millimeter radio-astronomical applications (either single-dish or interferometer). DLC and JG acknowledge support from STFC, in part through grant numbers ST/N000838/1 and ST/K001051/1. HD acknowledges financial support from the Spanish Ministry of Economy and Competitiveness (MINECO) under the 2014 Ramón y Cajal program MINECO RYC-2014-15686. This work would not have been possible without the long-term financial support from the Mexican Science and Technology Funding Agency, CONACYT during the construction and early operational phase of the Large Millimeter Telescope Alfonso Serrano, as well as support from the US National Science Foundation (NSF) via the University Radio Observatory program, INAOE and the University of Massachusetts, Amherst. LD, IO acknowledge support from the European Research Council AdvancedGrant, COSMICISM. LD also acknowledges support from ERC consolidator grant, CosmicDust. CY was supported by an ESO Fellowship. MJM acknowledges the support of the National Science Centre, Poland through the POLONEZ grant 2015/19/P/ST9/04010 and SONATA BIS grant 2018/30/E/ST9/00208; this project has received funding from the European Union's Horizon 2020 research and innovation programme under the Marie Skłodowska-Curie grant agreement No. 665778.

REFERENCES

Abolfathi B. et al., 2017, ApJS, 235, 42
Aravena M. et al., 2016, MNRAS, 457, 4406
Asboth V. et al., 2016, MNRAS, 462, 1989
Bakx T. J. L. C. et al., 2018, MNRAS, 473, 1751
Béthermin M. et al., 2017, A&A, 607, A89
Bianchi S., 2013, A&A, 552, 5
Blain A., 2002, Phys. Rep., 369, 111
Boone F. et al., 2013, A&A, 559, 5
Boone F. et al., 2015, Proc. IAU 11, z > 4 low luminosity dusty galaxy candidates in the Frontier Fields A2744, AS1063 and A370. Cambridge Univ. Press, Cambridge, p. 818
Bothwell M. S. et al., 2013, MNRAS, 429, 3047
Bourne N. et al., 2016, MNRAS, 462, 1714
Capak P. et al., 2008, ApJ, 681, L53
Capak P. L. et al., 2011, Nature, 470, 233
Carilli C., Walter F., 2013, ARA&A, 51, 105
Carlstrom J. E. et al., 2011, PASP, 123, 568
Casey C. M., Narayanan D., Cooray A., 2014, Phys. Rep., 541, 45161
Casey C. M. et al., 2018, ApJ, 862, 77
Chapin E. L. et al., 2009, MNRAS, 398, 1793
Chapin E. L. et al., 2011, MNRAS, 411, 505549
Chapin E. L., Berry D. S., Gibb A. G., Jenness T., Scott D., Tilanus R. P. J., Economou F., Holland W. S., 2013, MNRAS, 430, 2545
Chapman S. C., Blain A. W., Smail I., Ivison R. J., 2005, ApJ, 622, 772
Cheng T. et al., 2019, MNRAS, in press, doi:10.1093/mnras/stz2640
Clements D. L. et al., 2014, MNRAS, 439, 1193
Clements D. L. et al., 2018, MNRAS, 475, 2097
Combes F. et al., 2012, A&A, 538, 5
Coppin K. E. K. et al., 2009, MNRAS, 395, 1905
Cortese L. et al., 2014, MNRAS, 440, 942
Cox P. et al., 2011, ApJ, 740, 10
da Cunha E. et al., 2015, ApJ, 806, 22
Daddi E. et al., 2008, ApJ, 694, 1517
Danielson A. L. R. et al., 2010, MNRAS, 410, 1687
Dannerbauer H. et al., 2014, A&A, 570, A55
Diolaiti E., Bendinelli O., Bonaccini D., Close L. M., Currie D. G., Parmeggiani G., 2000,in Wizinowich P. L., ed, Proc. SPIE Conf. Ser. Vol. 4007, Adaptive Optical Systems Technology. SPIE, Bellingham, p. 879
Dowell C. D. et al., 2014, ApJ, 780, 75
Duivenvoorden S. et al., 2018, MNRAS, 477, 1
Dunne L., Eales S. A., Edmunds M. G., 2003, MNRAS, 341, 589
Eales S. et al., 2010, PASP, 122, 499
Egami E. et al., 2010, A&A, 518, L18

Downloaded from https://academic.oup.com/mnras/article/490/4/5317/5587004 by guest on 23 June 2022

Erickson N., Narayanan G., Goeller R., Grosslein R., 2007, in Baker A. J., Glenn J., Harris A. I., Mangum J. G., Yun M. S., eds, ASP Conf. Ser. Vol. 375, From Z-Machines to ALMA: (Sub)Millimeter Spectroscopy of Galaxies. Astron. Soc. Pac., San Francisco, p. 71
Foreman-Mackey D., Hogg D. W., Lang D., Goodman J., 2013, PASP, 125, 306
Fudamoto Y. et al., 2017, MNRAS, 472, 2028
Geach J. E. et al., 2017, MNRAS, 465, 1789
Goeller R. E., 2008, PhD thesis, Univ. Massachusetts Amherst
Goodman J., Weare J., 2010, Commun. Appl. Math. Comput. Sci., 5, 65
Greenslade J. et al., 2018, MNRAS, 476, 3
Greve T. R. et al., 2012, ApJ, 756, 101
Greve T. R. et al., 2014, ApJ, 794, 16
Gruppioni C. et al., 2017, Publ. Astron. Soc. Aust., 34, e055
Gullberg B. et al., 2018, ApJ, 859, 12
Harris A. I. et al., 2012, ApJ, 752, 152
Hayward C. C. et al., 2014, MNRAS, 445, 1598
Hughes D. et al., 2010, in Stepp L. M., Gilmozzi R., Hall H. J., eds, Proc. SPIE Conf. Ser. Vol. 7733, Ground-based and Airborne Telescopes III. SPIE, Bellingham, p. 773312
Hurley P. D. et al., 2016, MNRAS, 464, 885
Huynh M. T. et al., 2017, MNRAS, 467, 1222
Ikarashi S. et al., 2017, ApJ, 835, 286
Ivison R. J. et al., 2010, A&A, 518, 5
Ivison R. J. et al., 2016, ApJ, 832, 1
Jiménez-Andrade E. F. et al., 2018, A&A, 615, A25
Kennicutt R. C., 1998, ARA&A, 36, 189
Koprowski M. P., Dunlop J. S., Michałowski M. J., Coppin K. E. K., Geach J. E., McLure R. J., Scott D., van der Werf P. P., 2017, MNRAS, 471, 4155
Lapi A. et al., 2011, ApJ, 742, 24
Lawrence A. et al., 2006, MNRAS, 379, 1599
Liu D. et al., 2017, ApJ, 853, 172
Magnelli B. et al., 2012, A&A, 548, A22
Marrone D. P. et al., 2017, Nature, 553, 51
McMullin J. P., Waters B., Schiebel D., Young W., Golap K., 2007, in Shaw R. A., Hill F., Bell D. J., ASP Conf. Ser. Vol. 376, Astronomical Data Analysis Software and Systems XVI. Astron. Soc. Pac., San Francisco, p. 127
Michałowski M. J. et al., 2017, MNRAS, 469, 492
Miettinen O. et al., 2015, A&A, 577, A29
Miettinen O. et al., 2017, A&A, 606, A17
Monfardini A. et al., 2010, A&A, 521, A29
Murray N., 2010, ApJ, 729, 14
Neri R., Downes D., Cox P., Walter F., 2014, A&A, 562, A35
Novak M. et al., 2017, A&A, 602, A5
Oliver S. J. et al., 2012, MNRAS, 424, 1614
Oteo I. et al., 2016a, ApJ, 827, 11
Oteo I., Zwaan M. A., Ivison R. J., Smail I., Biggs A. D., 2016b, ApJ, 837, 9
Papadopoulos P. P., van der Werf P., Xilouris E., Isaak K. G., Gao Y., 2012, ApJ, 751, 10
Pearson E. A. et al., 2013, MNRAS, 435, 2753
Polletta M. et al., 2007, ApJ, 663, 81
Rangwala N. et al., 2011, ApJ, 743, 94
Riechers D. A. et al., 2010, ApJ, 720, L131
Riechers D. A. et al., 2013, Nature, 496, 329
Riechers D. A. et al., 2017, ApJ, 850, 1
Roseboom I. G. et al., 2010, MNRAS, 409, 48
Rowan-Robinson M. et al., 2016, MNRAS, 461, 1100
Sahai R., Nyman L.-Å., 1997, ApJ, 487, L155
Schiminovich D. et al., 2007, ApJS, 173, 315
Schneider N. et al., 2014, A&A, 578, 17
Scudder J. M., Oliver S., Hurley P. D., Griffin M., Sargent M. T., Scott D., Wang L., Wardlow J. L., 2016, MNRAS, 460, 1119
Simpson J. M. et al., 2017, ApJ, 839, 58
Simspon J. M., et al., 2019, ApJ, 880, 43
Smith D. J. B., Hayward C. C., Jarvis M. J., Simpson C., 2017, MNRAS, 471, 2453
Strandet M. L. et al., 2016, ApJ, 822, 80
Strandet M. L. et al., 2017, ApJ, 842, 2
Swinbank M. et al., 2010, Nature, 464, 733
Tacconi L. J. et al., 2010, Nature, 463, 781
Taylor M. B., 2005, in Shopbell M. , Britton M., Ebert R., eds, ASP Conf. Ser. Vol. 347, Astronomical Data Analysis Software and Systems XIV. Astron. Soc. Pac., San Francisco, p. 29
The Astropy Collaboration A., 2013, A&A, 558, 9
Valiante E. et al., 2016, MNRAS, 462, 3146
Vieira J. D. et al., 2013, Nature, 495, 344
Walter F. et al., 2012, Nature, 486, 233
Wang R. et al., 2013, ApJ, 773, 44
Wardlow J. L. et al., 2011, MNRAS, 415, 1479
Warren S. J. et al., 2006, MNRAS, 375, 213
Weiß A. et al., 2013, ApJ, 767, 88
Wilkinson A. et al., 2016, MNRAS, 464, 1380
Yang C. et al., 2017, A&A, 608, 41
Yun M. S. et al., 2015, MNRAS, 454, 3485
Zavala J. A. et al., 2018, Nature Astron.,

APPENDIX: THE NIKA OBSERVATIONS

During the course of our analysis, and as can be seen directly in Fig. 9, it became apparent that the NIKA fluxes appeared systematically lower than expected by a factor of ∼1.5. Examination of the processed data, $\tau_{225\,\mathrm{GHz}}$ values during the observations, and observing logs do not suggest issues or any likely origin for any possible systematic errors. The data were taken during a shared-risk mode, and the pipelines to reduce the raw data are no longer available, so it is not possible to re-reduce the data. Nevertheless, comparison to data taken at other wavelengths appear to indicate a systematic offset beyond the reported errors, of around 50 per cent.

Because of these discrepancies, we also ran our sampler without the NIKA data included to see what effects it has on our results. The results of excluding the data are shown in Figs A1 and A2. The derived parameters end up similar, though parameters are slightly higher when excluding the NIKA data. Both models are consistent with an optically thin model (i.e. for all observed frequencies observations $\frac{\nu}{\nu_0} << 1$), have similar derived FIR luminosities ($\log_{10}(L_{\mathrm{FIR}}/\mathrm{L}_\odot) = 12.86^{+0.25}_{-0.94}$ when excluding the NIKA data), and similar predicted dust masses ($\log_{10}(M_{\mathrm{dust}}/\mathrm{M}_\odot) = 8.88^{+0.82}_{-0.50}$ when excluding). The only clear differences are in the derived β values, which are $\beta = 1.23^{+0.20}_{-0.15}$ when including the NIKA data but $\beta = 1.79^{+0.53}_{-0.38}$ when excluding the NIKA data, and in the $\mathrm{T}_{\mathrm{dust}}/(1+z)$ parameters, which when including the NIKA data are $\mathrm{T}_{\mathrm{dust}}/(1+z) = 6.22 = 3^{+0.96}_{-0.84}$ compared to $\mathrm{T}_{\mathrm{dust}}/(1+z) = 4.87^{+1.34}_{-1.21}$ without. Additionally, the reduced χ^2 values for the median sampled parameters is $\chi^2_{\mathrm{red}} = 3.95$ when including the NIKA data, but 2.62 when excluding it, indicating marginally better fits. This difference, however, does not appear to be having a significant effect on most of the derived parameters for NGP6_D1, with primary differences emerging at the shortest ($\lambda < 500\ \mu$m) wavelengths, where more data are required in order to resolve this potential conflict. In this paper, we continue to include the NIKA data, but we note that it is possible that β values may be higher, whilst $\mathrm{T}_{\mathrm{dust}}/(1+z)$ values might be lower.

Downloaded from https://academic.oup.com/mnras/article/490/4/5317/5587004 by guest on 23 June 2022

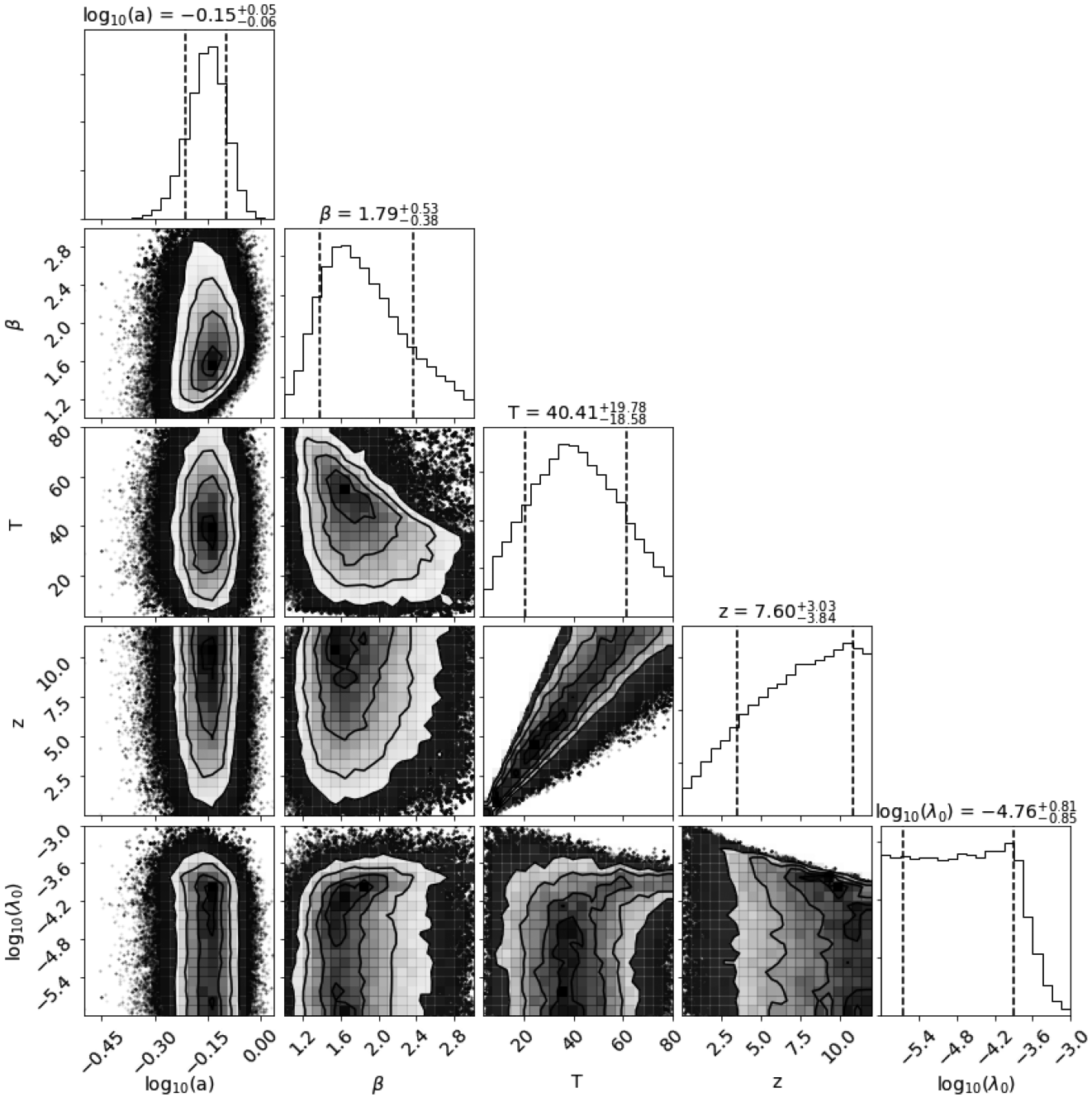


Figure A1. The same as Fig. 8, but excluding the NIKA data.

Downloaded from https://academic.oup.com/mnras/article/490/4/5317/5587004 by guest on 23 June 2022

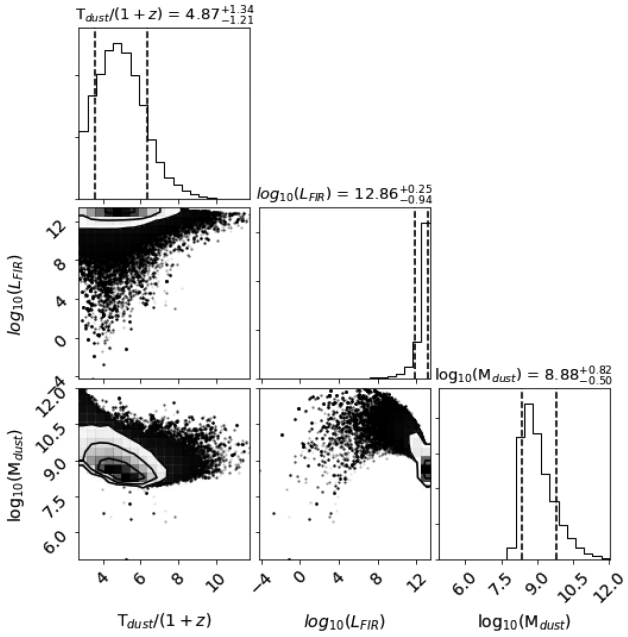


Figure A2. The same as Fig. 10, but excluding the NIKA data.

This paper has been typeset from a TEX/LATEX file prepared by the author.

Downloaded from https://academic.oup.com/mnras/article/490/4/5317/5587004 by guest on 23 June 2022